

Stereoisomeric selection upon adsorption: A structural and optical study of curcuminoid derivatives on ultrathin films of KCl on Au(111) and on bulk KCl(001)

Thomas Leoni ^{1,*}, Laurent Nony^{2,*}, Elena Zaborova,¹ Sylvain Clair ², Frédéric Fagès,¹ Franck Para,² Alain Ranguis,¹ Conrad Becker ¹ and Christian Loppacher ²

¹Aix Marseille Univ, CNRS, CINaM, UMR 7325, Marseille, France

²Aix Marseille Univ, CNRS, IM2NP, UMR 7334, Marseille, France

 (Received 14 July 2021; revised 20 September 2021; accepted 12 October 2021; published 9 November 2021)

We present a combined scanning tunneling microscopy (STM), noncontact atomic force microscopy (nc-AFM), and differential reflectance spectroscopy (DRS) study aiming at the characterization of the relationship between structural and optical properties of a supramolecular assembly of a curcuminoid derivative adsorbed on two kinds of substrates: bilayers of KCl on Au(111) [2 ML KCl/Au(111)] and KCl(001) bulk. The molecule features a difluoroboron (BF₂) complex as well as cyano (CN) end groups, which induces an internal dipole moment of a few Debyes. The comparative study of the structural properties of the molecules adsorbed on 2 ML KCl/Au(111), which allows for STM characterization, and KCl bulk, which allows for nc-AFM and DRS characterization, shows that the molecular adsorption is similar on both substrates. STM and nc-AFM give evidence that the on-surface condensation of the molecules into supramolecular assemblies is steered by two main interactions: the molecule-substrate interaction between the CN end groups of the molecule and the cationic K⁺ species, as well as an in-plane intermolecular interaction involving BF₂ and phenyl groups. Based on density functional theory calculations, we propose an epitaxial molecular structure described by a two-molecule unit cell forming an 8 × 2 supercell on the KCl surface that grows in form of ribbons along the (100) or (010) directions of the substrate, which are polar. Among several possible stereoisomers for the molecule, it is found that the balance between vertical and in-plane interactions selects the one whose size matches the distance between K⁺ species to condense on the substrate and not the most stable one stemming from the gas phase. Finally, optical spectroscopy in solvent and DRS measurements performed on the supramolecular assembly exhibit similar features identified as three absorption peaks tracing a $\pi \rightarrow \pi^*$ electronic transition followed by a vibronic progression, plus a broader band featuring a set of higher-energy transitions. Due to both the weak electrostatic interactions and a lack of π - π interactions in the condensed molecular phase, DR spectra exhibit no major excitonic effect, but a nonrigid redshift of the molecular absorption band compared to the situation in solvent. This observation is found to be consistent with the isomer selection due to the transition from the gas phase to the on-surface condensed phase.

DOI: [10.1103/PhysRevB.104.205415](https://doi.org/10.1103/PhysRevB.104.205415)

I. INTRODUCTION

Ordered nanostructures formed by spontaneous assembly of organic molecules adsorbed on solid substrates have been investigated since the early 1990s by scanning probe methods such as scanning tunneling microscopy (STM), or atomic force microscopy (AFM), in ultrahigh vacuum (cf. Refs. [1–14], to cite a few). These pioneer studies were either carried out on individual molecules, or molecular assemblies in the monolayer (ML) regime, adsorbed on single-crystal metal substrates and semiconductors by STM. With these substrates, it was quickly pointed out that coupling effects and charge transfer between the surface electronic states and those of the molecules took place, which did not only influence the adsorption configuration of the molecules, but also their intrinsic functional properties [7,15].

Following the technical and experimental developments of noncontact AFM (nc-AFM), the studies of organic nanos-

tructures adsorbed on solid surfaces were extended to bulk dielectrics in the beginning of the 2000s, down to the molecular scale (cf. Refs. [16–27], to cite a few). The use of weakly reactive dielectric substrates, as opposed to metals or semiconductors, preserves or hardly influences the intrinsic properties of the nanostructures without a significant charge transfer. However, in this case, the substrates prevent the use of STM, which makes the study of the electronic properties of the adsorbed nanostructures difficult. Besides, when operated at room temperature, nc-AFM is both slower, more demanding, and usually offers poorer spatial resolution (molecular resolution only) as compared to STM [intramolecular local density of states (LDOS) contrast].

In the 2000s, to circumvent the limitations due to bare metallic substrates, Repp *et al.* proposed an alternative [15,28,29]. The idea was to use thin layers of NaCl (two monolayers typically), a large-gap material of 8.5 eV, grown on the surface of the metallic single crystal for the adsorption of the molecules. In Ref. [15], Repp *et al.* report results obtained with Cu(111) and Cu(100) single crystals as substrates. It was then shown that with these heterosurfaces, the gain is

*These authors contributed equally to this work.

†Corresponding author: thomas.leoni@univ-amu.fr

twofold. First, the interstitial dielectric layers are thin enough to allow for electrons to tunnel from the tip (metallic substrate) to the metallic substrate (tip) through the 2 ML NaCl tunnel barrier at a current that remains detectable (pA regime). Thus, STM can still be used reliably. Second, the dielectric layers act as physical spacers between the molecules and the substrate, which electronically decouples them from the metallic states, nearly as efficiently as with bulk dielectrics.

This approach triggered many studies focused on the adsorption of individual atoms [30], individual molecules [14,31], or of organic films [32]. Regarding the dielectric layers, other inorganic heterospacers were used as well, such as oxide thin films [33–35]. But except the case of 2 ML NaCl, the use of other alkali halide thin films (LiF, KBr, KCl, RbCl, ...) was rarely reported.

Among alkali halides, KCl is of particular interest. On bulk KCl(001), comparative nc-AFM studies have shown that molecules carrying cyano groups (CN) develop a specific interaction with the K^+ ions [36–39] that is able to steer the epitaxial growth of the supramolecular assembly. The resulting supramolecular networks are usually extended and highly ordered, an important property when investigating organic layers on surfaces. Assemblies with equivalently good crystallinity are rarely observed when using other substrates than KCl(001). Although the detailed mechanisms of that specific interaction remain to be clarified, the balance between the large polarizability of the CN moieties allowing for their anchoring on the cationic sites, along with the moderate surface corrugation [40] allowing for a sufficiently large molecular diffusion length to form extended assemblies, are pointed out.

Regarding the thin-film regime, KCl thin films were reported on metals such as Ag(001) [41,42], Au(111) [43,44], Cu(100) [45], and Cu(111) [44]; on semiconductors such as Ge(001) [46], Si(100)- 2×1 [47], and Si(111) 7×7 [48]; and on bulk alkali halide surfaces such as NaCl(001) [49,50].

If the optical properties of the adsorbed molecules are targeted, their optical absorption can be investigated by means of *in situ* differential reflectance spectroscopy (DRS) with a sensitivity, including anisotropic sensitivity, down to a fraction of a monolayer [51–54]. DRS can also be coupled to *in situ* fluorescence, or vibrational spectroscopy [55–57]. However, such a study can not be carried out on a metal substrate due to the hybridization of the metallic states with the molecular orbitals, which is known to promote the quenching of the photoluminescence at the organic-metal interface. Again, ultrathin dielectric films deposited on the metal substrate can be used to efficiently overcome the quenching [34,55–57]. For instance, Müller *et al.* have reported remarkable results of vibrational spectroscopy on perylene-3,4,9,10-tetracarboxylic acid dianhydride (PTCDA) adsorbed on epitaxial KCl films on Ag(100) at 20 K, where individual vibronic modes of the molecules were resolved with a resolution of 20 cm^{-1} (2.5 meV) only [41,58,59].

The analysis of the DR spectra permits to extract the dielectric function of the adsorbed layers, as well [60]. But here again, the use of a metallic substrate is challenging. Indeed, as detailed in Ref. [60], the nonlinear nature of Fresnel equations makes the interpretation of the DR spectra tedious. Assuming the imaginary part of the dielectric function of the substrate as a constant greatly simplifies the approach, which is not the

case with metals whose absorption in the UV-visible range is much structured [61,62]. Even in the case of a metallic substrate including an ultrathin dielectric spacer, the disentangling of the dielectric functions of the stratified medium (molecular adlayer/ultrathin spacer/metallic substrate) out of the DR spectra is demanding and requires dedicated methods (transfer matrix ...). Conversely, bulk alkali halide single crystals offer the advantage of being transparent, with a weak, nearly constant, optical absorption in the UV-visible range. Therefore, they offer a unique opportunity to investigate the coupling between structural and optical properties of the molecular assemblies grown at their surface.

In summary, if a comprehensive study of structural, electronic, and optical properties of organic assemblies adsorbed on a surface is targeted, a rational methodology consists in the following: (1) selecting a KCl substrate as it seems quite versatile for molecular adsorption, (2) selecting a molecular dye absorbing in the UV-visible range and carrying peripheral CN moieties, and (3) combining the types of substrates 2 ML KCl/metal and bulk KCl(001). Regarding the investigation methods, STM is to be applied on the 2 ML KCl/metal substrate to investigate the structural and electronic properties of the assemblies, nc-AFM and DRS on KCl(001) to investigate their structural and optical properties. Combined with Kelvin probe force microscopy (KPFM), nc-AFM could also provide insights in the electronic properties of the assemblies on both types of samples.

The above methodology raises two major issues. On the one hand, one must find a metal onto which the bilayer of KCl grows with a similar structure to that of the bulk. On the other hand, to make the study consistent, one must make sure that the molecular assemblies are structurally similar between 2 ML KCl/metal and bulk KCl(001).

Following the purpose of our study, we selected a molecular dye substituted with CN end groups based on a curcuminoid derivative. The dye displays a diarylheptanoid backbone and represents a particular case of β -diketonate ligands [63]. We focused on the difluoroboron β -diketonate complex that features an important family of photoactive and electroactive molecules with optical [64–68] and electrochemical [66,69,70] properties. Owing to their extended π -conjugated structure, the difluoroboron complexes of curcuminoid derivatives exhibit strong visible absorption and fluorescence [71–73], and unique near-infrared emission in both solution and in the solid state [74,75]. The former property stems from the combination of electron donor (D) and acceptor (A) units in a D-A-D quadrupolarlike architecture of the molecule, in which “A” is the central dioxaborine ring and “D” is a terminal aromatic moiety acting as an electron donor substituent. These molecules are known to be versatile fluorophores [65,67,68] and electron acceptors [76,77]. They are used as charge transport materials in organic photovoltaics and optoelectronics such as organic field effect transistors and organic light-emitting diodes [78–80], in bioimaging [81], and in nonlinear optics as well [71,73,74].

In this work, we report a set of structural and optical analyses on the above-mentioned curcuminoid derivative adsorbed in the sub-ML regime on two types of substrates: 2 ML KCl/Au(111) and bulk KCl(001), onto which the molecules form a well-developed supramolecular assembly. On 2 ML

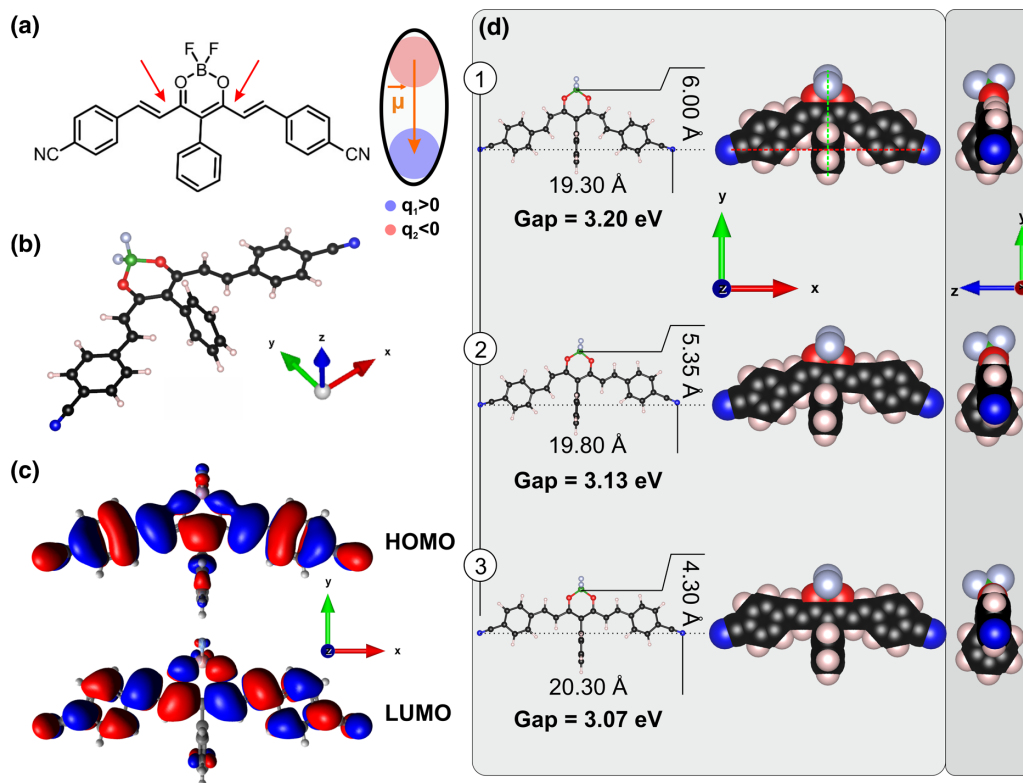


FIG. 1. (a) Scheme of the Curc-di(CN) molecule. The red arrows indicate the bonds around which the ethylenic groups can rotate to form stereo isomers [as shown in (d)]. The orientation of the DFT-calculated internal dipole moment of the molecule (cf. text), of strength μ , is depicted by the orange arrow. (b) Perspective view of the isomer 1 of the molecule, as reported in (d). (c) Highest occupied and lowest unoccupied molecular orbitals (HOMO and LUMO, respectively) for the isomer 3 shown in (d3), as calculated by DFT (cf. text). (d) Balls-and-sticks and space-filling models of the relaxed configurations of three isomers of the molecule derived by rotation of the ethylenic moieties with respect to the σ bond stressed in (a), as calculated by DFT. The HOMO-LUMO gap has been reported for each isomer. For isomer 1, the long (red dotted line) and short (green dotted line) molecular axes are drawn.

KCl/Au(111), the structural properties of the assemblies are characterized by STM at low temperature (liquid-helium and liquid-nitrogen temperature). On KCl(001), the structural and optical properties of the assemblies are characterized by nc-AFM/KPFM and DRS (room temperature).

The paper is organized as follows. In Sec. II, the molecule, the substrates, and the methods are introduced. Section III presents the results that have been split into four subsections. In the first one, we detail the structure of the 2 ML KCl/Au(111) substrate. In the second and third subsections, the structural properties of the supramolecular assemblies on 2 ML KCl/Au(111) and bulk KCl(001) are detailed, respectively. The former are acquired by STM and the latter by joint nc-AFM/KPFM measurements. In the last subsection, the optical absorption properties of the molecules in solvent are detailed and compared to those of the molecules adsorbed on bulk KCl(001), as measured by DRS. The results are combined and discussed in Sec. IV.

II. MATERIALS AND METHODS

A. Curc-di(CN) molecule

The molecule used in this study is a 4,6-bis[(E)-4-cyanostyryl]-2,2-difluoro-5-phenyl-2H-1,3,2-dioxaborinin-1-ium-2-uide [hereafter referred to as

Curc-di(CN), cf. Fig. 1]. Its synthesis has been reported in Ref. [82]. Curc-di(CN) is the difluoroboron complex of a curcuminoid derivative in which the para position of the two-terminal phenyl rings features a cyano group (“D” moieties). The central position of the curcuminoid backbone, hereafter called the meso position, is substituted with a phenyl group. The geometry of the molecule favors the creation of an internal dipole moment whose strength can be tuned upon the electronegativity of the terminal moiety of the side groups [cf. Figs. 1(a) and 1(b)].

Several stereoisomers of the molecule can be considered, whose sizes and dipole moments differ, as confirmed by density functional theory (DFT) calculations (cf. hereafter). We will focus on three of them which are helpful to discuss our results [cf. Fig. 1(d)]. These are derived from rotations of the side groups along the σ bonds indicated by the red arrows in Fig. 1(a), while keeping a transconfiguration of the double bond inside the side group. In configuration 1 [cf. Fig. 1(d1)], both side groups are referred to as pointing “downwards” (following the orientation of the double bond). For each isomer, it is useful to define two reference axes to discuss its adsorption configuration, illustrated in Fig. 1(d1) with the isomer 1. We thus define the long axis of the molecule as the axis joining its N atoms [x axis, cf. red dotted line in Fig. 1(d1)] and the short axis as the symmetry axis of the molecule [perpendicular to

the former one, y axis, cf. green dotted line in Fig. 1(d1)]. For isomer 2 [cf. Fig. 1(d2)], side groups have alternated orientations, with one pointing downwards, the other one pointing “upwards.” With isomer 3 [cf. Fig. 1(d3)], both side groups point upwards.

B. DFT calculations

Density functional theory calculations at the gas phase were carried out to evaluate the geometric structures of the different isomers using B3LYP [83] hybrid functional and 6-311 basis set implemented in GAUSSIAN 16 [84] and in ORCA [85] software packages.

The relaxed configurations and partial charges of each isolated isomer are reported in Fig. 1(d). Isomer 3 was found to be the most stable structure, while isomers 2 and 1 are higher in energy by, respectively, 0.22 and 0.47 eV. For isomer 1 to 3, the distances between N moieties are estimated to be $\simeq 19.3$, $\simeq 19.8$, and $\simeq 20.3$ Å, respectively. In the perpendicular direction, the distances from B to N atoms, as indicated in Fig. 1(d), are $\simeq 6.0$, $\simeq 5.4$, and $\simeq 4.3$ Å, respectively. The relaxed configurations show that each isomer remains quite planar, except for (i) the fluorine atoms which protrude from both sides of the mean plane of the molecule due to the sp^3 hybridization of the boron and (ii) the mesophenyl which aligns perpendicularly with respect to the mean plane of the molecule.

From the relaxed configuration of isomer 3, the highest occupied molecular orbital (HOMO) and lowest unoccupied molecular orbital (LUMO) have been calculated and are reported in Fig. 1(c). The calculated HOMO-LUMO gap is indicated under each isomer in Fig. 1(d).

The DFT calculations have revealed a good flexibility for the various isomers with an increase in energy of no more than 100 meV when the distance between N atoms was varied by ± 0.5 Å around their minimum energy configuration.

The calculated dipole moment $\vec{\mu}$ of the molecules [orange arrow in Fig. 1(a)], oriented along or close to the y axis, amounts to $\mu_1 = 8.4$ D, $\mu_2 = 7.3$ D, and $\mu_3 = 6.3$ D for the three isomers, respectively.

Finally, in Fig. 1(c), the isomers have been represented with a balls-and-sticks model and a space-filling model, which is helpful to discuss our results.

C. Substrates

Au(111) single crystals were cleaned by repeated cycles of sputtering (1 keV) annealing (550 °C). 2 ML KCl were subsequently deposited on the Au(111) surface kept at room temperature by sublimation at 420° of small fragments of a KCl(001) single crystal loaded into the quartz crucible of a Knudsen cell during 20 min.

The KCl(001) single crystal (MaTecK GmbH, 52428 Jülich, Germany) was cleaved *ex situ*, quickly introduced into the preparation chamber of a UHV setup consisting of two interconnected chambers (preparation and analysis, base pressure $\simeq 10^{-10}$ mbar), and annealed to 240 °C during 1 h in order to obtain atomically clean surfaces with large terraces.

Curc-di(CN) molecules were deposited *in situ* onto the substrates kept at room temperature (RT) by sublimation from quartz crucibles. The rate of deposition was calibrated

by a quartz crystal microbalance connected to a counter (TTi, TF930) and a homemade LABVIEW program allowing for both the control and the monitoring of the evaporation rate. Molecular deposits were performed with a typical flux of 1 ML/3 min. The crosscheck between the evaporation rate, the exposure time of the sample to the flux, and the STM or nc-AFM images allows for an estimation of the coverage rate of the molecules on the surface with an accuracy of 10%.

D. Scanning tunneling microscopy, noncontact atomic force microscopy, and Kelvin probe force microscopy

The scanning tunneling microscopy (STM) experiments were performed both at liquid-nitrogen temperature ($\simeq 78$ K) and liquid-helium temperature ($\simeq 4.8$ K) in ultrahigh vacuum environment on an Omicron LT-SPM with bias voltage applied on the sample and operating in constant-current mode. The STM images were processed and analysed with GWYDDION [86].

The noncontact AFM experiments were carried out at RT with a commercial Omicron VT-AFM equipped with a home-built detection electronics and a R9 RHK controller (RHK Technology Inc., Troy, MI 48083, USA). The VT-AFM is part of the analysis chamber of the UHV setup. Kelvin probe force microscopy (KPFM) was engaged during the acquisition of nc-AFM images to compensate electrostatic forces and yield consistent contact potential difference (CPD) images. CPD measurements were performed in FM-KPFM mode with a 2345-Hz modulation frequency detected on the side bands of the central frequency of the cantilever. The AC bias modulation was 1 V. Nanosensor cantilevers were used (PPP-NCL with resonance frequency $f_0 = 157.760$ kHz, spring constant $k_0 \simeq 30$ N/m, quality factor $Q = 40\,000$) at oscillation amplitudes $A_0 \simeq 2$ nm and frequency shifts $\Delta f \simeq -20$ Hz, hence a normalized Δf [87]: $\gamma = k_0 A_0^{3/2} \Delta f / f_0 \simeq -0.01$ nN $\sqrt{\text{nm}}$.

Experimental nc-AFM images were analyzed using the WSEX software [88]. The data have been acquired and repeated over several weeks with various samples and tips. The reported images are mostly representative of our results whose statistics is robust. A thorough set of postprocessing including cross correlation, fast Fourier transform (FFT), drift-correction procedures, histograms, and corresponding Gaussian fits allowed us to quantify our measurements with typical 5%-error bars.

E. Absorption spectroscopy

The UV-visible absorption properties of the Curc-di(CN) molecule were measured in several aprotic solvents in order to avoid any specific solute-solvent interaction, namely, acetone, dichloromethane (DCM), tetrahydrofuran (THF), ethyl acetate (AcOEt), diethyl ether (Et₂O), dibutyl ether (Bu₂O), chloroform (CCl₄), and cyclohexane. All solvents were of spectroscopic grade. The concentration of the solutions was 10^{-5} M. The UV-visible absorption spectra in solution were measured on a Varian Cary 50.

The properties of those solvents span from weakly dispersive and apolar (Et₂O, cyclohexane) to strongly dispersive and polar (acetone), ethyl acetate, and chloroform being intermediate. In apolar, aprotic, and weakly dispersive solvents, the

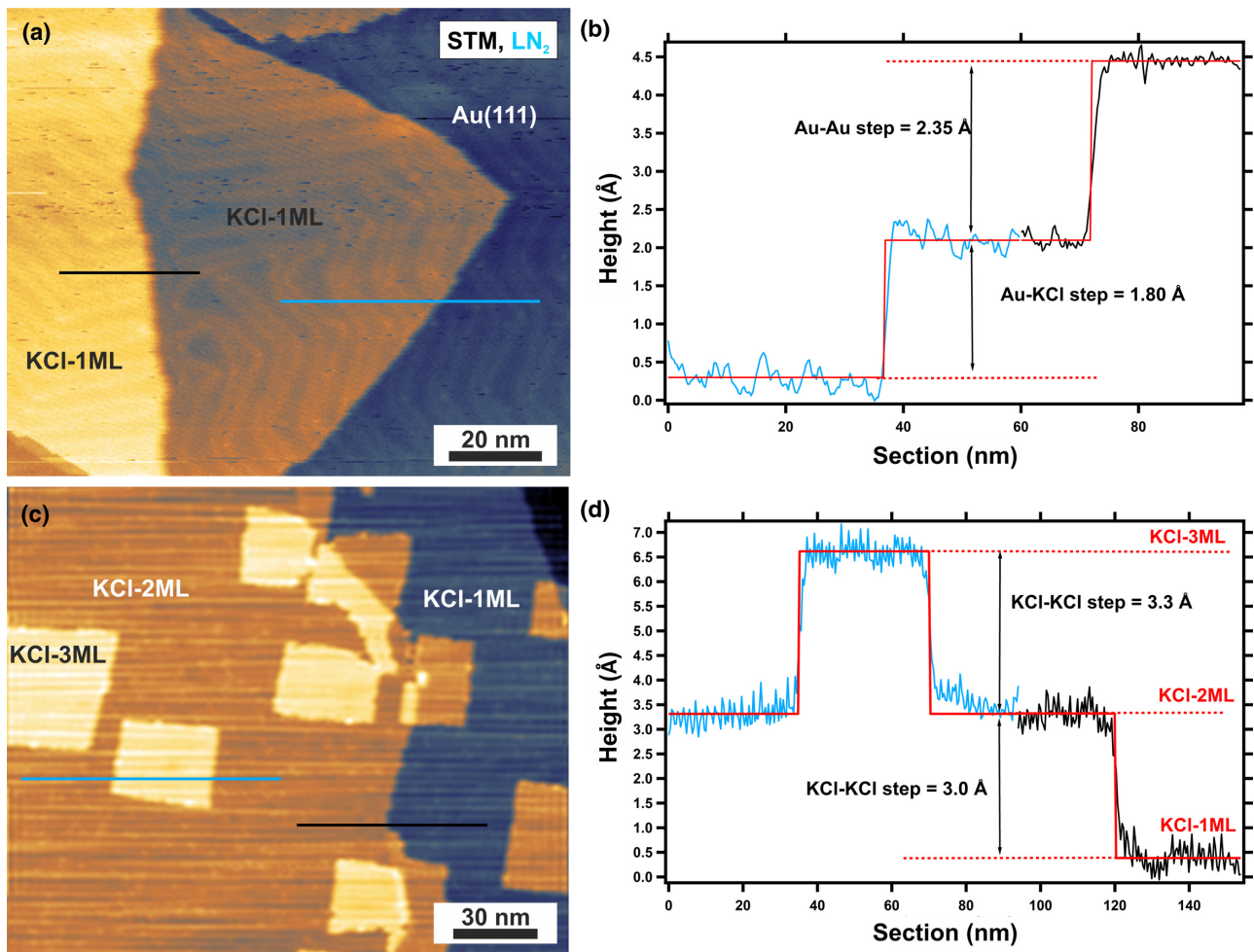


FIG. 2. STM images and profiles analysis of KCl islands on Au(111) at 78 K. (a) STM image of 1 ML KCl/Au(111). $I_t = 2$ pA, $V_b = -3$ V. The first KCl layer consists of square-shaped islands with a carpetlike behavior. (b) Height profiles taken from (a). The blue height profile is measured along a Au-KCl step. The black one is along a Au-Au step. The red line is obtained by fitting the experimental profiles with the step edge function of GWYDDION [86]. (c) STM images of the second and third KCl layer. $I_t = 3$ pA, $V_b = 4.5$ V. (d) Height profile taken from (b). The blue height profile is measured between the second and the third KCl island. The dark profile is measured between the first and the second KCl island.

spectra are expected to be more representative of the absorption of molecules in the gas phase.

F. Differential reflectance spectroscopy

Differential reflectance spectroscopy (DRS) is a nondestructive, UV-visible near-IR spectroscopic method able to measure in real time and with a high sensitivity the change of reflectance $R(\lambda)$ on a substrate upon adsorption of a molecular adlayer. Assuming an adlayer of thickness d , then the DRS signal is defined as

$$\text{DRS}(\lambda, d) = \frac{R(\lambda, d) - R(0)}{R(0)}, \quad (1)$$

$R(0)$ being the reflectance of the bare substrate. The differential aspect of the measure gives access to the changes of reflectance due to adlayers with a sensitivity to the submonolayer regime [51–54,60,89].

The theoretical context of DRS is the Fresnel equations describing the pathway of the light through the stratified medium (adlayers and substrate) coupled to the microscopic description of the dielectric function of the adlayer, of tensorial nature. Thus, the structure of the DR spectra possesses a large degree of complexity. Nevertheless, in the limit of a homogeneous molecular adlayer (similar molecules, identically adsorbed and periodically arranged), whose thickness is much smaller than the illumination wavelength ($d \ll \lambda$), it was shown that DR spectra scale linearly with d and the imaginary part of the dielectric function of the adlayer $\tilde{\epsilon}_{\text{mol}}(\lambda) = \epsilon'_{\text{mol}}(\lambda) - i\epsilon''_{\text{mol}}(\lambda)$. In this regime, the DRS signal also relates to the absorbance $A(\lambda, d)$ of the molecular adlayer, as measured by regular absorption spectroscopy, namely [51],

$$\begin{aligned} \text{DRS}(\lambda, d) &= -\frac{8\pi d \cos(\theta)}{\lambda(n_s^2 - 1)} \text{Im}\{\tilde{\epsilon}_{\text{mol}}(\lambda)\} \\ &= \frac{4 \ln(10)}{n_s^2 - 1} \text{Re}\{\sqrt{\tilde{\epsilon}_{\text{mol}}(\lambda)}\} A(\lambda, d), \end{aligned} \quad (2)$$

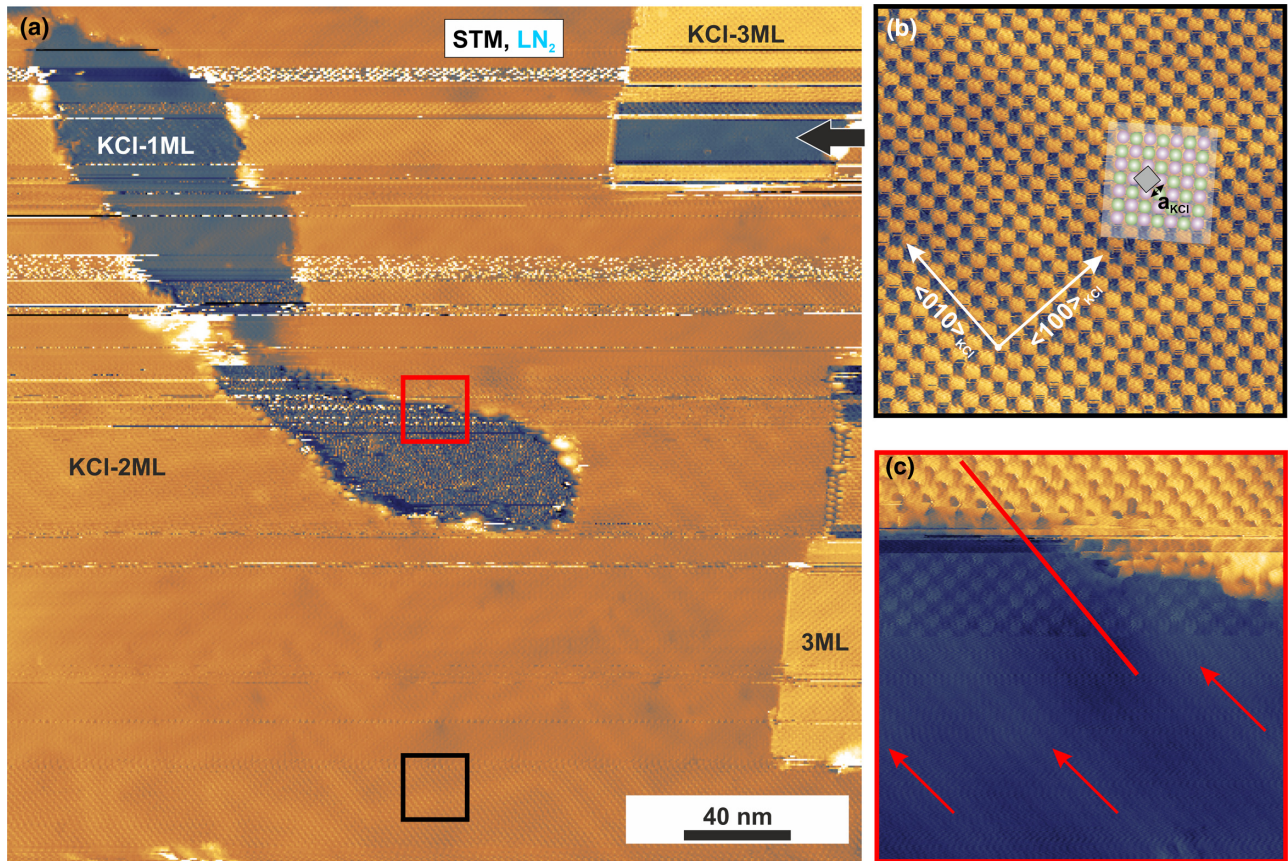


FIG. 3. STM images of KCl islands on Au(111) at 78 K. (a) STM image on the first three KCl monolayers with occasional contrast inversion on the third layer (black arrow). $I_t = 5$ pA, $V_b = 1.2$ V. (b) STM image of the black square shown in (a). The atomic resolution gives the direction of the $\langle 100 \rangle_{\text{KCl}}$ and $\langle 010 \rangle_{\text{KCl}}$ crystallographic axes of the layer. An atomistic scheme of the KCl arrangement has been overlaid wherein the primitive KCl unit cell is highlighted. $I_t = 5$ pA, $V_b = 1.2$ V, $10 \text{ nm} \times 10 \text{ nm}$. (c) STM image of the red square shown in (a). The step separating the first (blue) and the second (yellow) layer is resolved with atomic precision and confirms a growth of KCl according to a regular fcc pattern. The herringbone reconstruction of gold is visible underneath the first layer (red arrows) and aligned with the $\langle 010 \rangle_{\text{KCl}}$ direction. $I_t = 5$ pA, $V_b = 1.2$ V $10 \text{ nm} \times 10 \text{ nm}$.

where θ and n_s are the incidence angle of the light with respect to the normal to the substrate and its refractive index, respectively.

To allow for the acquisition of the DR spectra during the sublimation of the molecules (typically 20 min), our DRS setup is implemented in the preparation chamber of the UHV setup including the VT-AFM. Unpolarized, white light is focused by means of a set of *ex situ* lenses towards the sample which is kept at RT while the sublimation takes place. The reflected light is collected *ex situ* using a spectrometer allowing for the real-time monitoring of the DRS signal. More details (geometry, data acquisition, and postprocessing) can be found in Refs. [60,90].

Once the targeted number of molecular layers to be deposited is achieved, the molecular flux is stopped. Nevertheless, we keep acquiring DR spectra during 10 additional minutes to monitor whether changes in the spectra occur that might trace potential kinetics effects of the molecules at the surface. In the present case, no substantial change of the DR spectra was noticed during this lapse of time.

III. RESULTS

A. Morphological characterization of KCl thin films on Au(111)

After sublimation of KCl onto a clean Au(111) surface kept at room temperature, square-shaped KCl islands are visible on the bare Au(111), as revealed by the STM images acquired at the temperature of liquid nitrogen (cf. Fig. 2). Height profile analyses derived from Fig. 2(a) show that the first KCl adlayer, hereafter referred to as 1 ML KCl, has an apparent height of 1.8 \AA (cf. Fig. 2(b)), while the Au-Au step height is measured at 2.35 \AA , close to the expected structural value of 2.38 \AA . The apparent height of the 1 ML KCl is smaller than the potassium van der Waals radius (2.8 \AA). However, as many times observed, on the first layers of alkali halide thin films on metal, measured apparent heights in STM underestimate the geometrical height due to the insulating character of the thin film [91,92]. When the tip is above this insulating layer, tunneling electrons encounter a double-barrier tunnel junction formed by the vacuum and the KCl layer and in order to maintain the current constant, the tip-sample distance position is reduced compared to the situation where the tip is above the bare Au(111) surface.

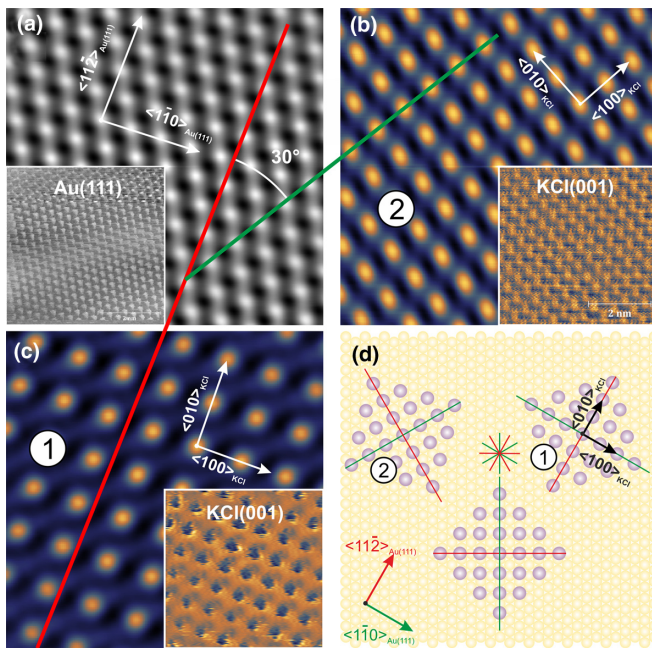


FIG. 4. Relative crystallographic orientation of KCl domains with respect to the Au(111) surface acquired in STM at 4.8 K. (a) Autocorrelation of the atomically resolved Au(111) STM image shown in inset. Green and red lines indicate the $\langle 1\bar{1}0 \rangle_{\text{Au}}$ and $\langle 11\bar{2} \rangle_{\text{Au}}$ directions, respectively. (b) Autocorrelation of the atomically resolved STM image shown in inset measured on a KCl domain. On this domain, the $\langle 100 \rangle_{\text{KCl}}$ direction is aligned with the green line. (c) Autocorrelation of the atomically resolved STM image shown in inset measured on another KCl domain located several tens of microns away from the former. Here, the $\langle 010 \rangle_{\text{KCl}}$ direction is aligned with the $\langle 11\bar{2} \rangle_{\text{Au}}$ direction. We note an angle of 30° between this domain and the one in image (b). (d) Scheme of the three possible crystallographic variants for the KCl domains in epitaxy with the Au(111) surface.

Yet, we conclude that the KCl wetting layer consists of a monatomic plane of KCl with a carpetlike growth mode, as seen in Fig. 2(a) where the layer spans over a monatomic step of the Au(111) surface. In this figure, the Au(111) herringbone reconstruction remains clearly visible underneath the first monolayer of KCl. STM images [cf. Fig. 2(c)] show that the second (2 ML) and third (3 ML) KCl layers start to form before completion of the wetting layer, while remaining square shaped. Height profile analyses [cf. Fig. 2(d)] show a (3.0 ± 0.3) Å step height between the first and the second layers, and a (3.3 ± 0.3) Å step height between the second and third layers. In this case, apparent heights are in better agreement with the expected geometrical heights. It is probably an effect due to the high bias voltage applied (4.5 V). Apparent height strongly depends on the applied bias, as previously shown and explained on NaCl/Cu(001) [93], NaCl/Au(111) [92], NaCl/Ag(100) [94], or NaCl/Cu(311) [91]. At high bias voltage, the contribution of additional electronic states increases the tunneling current causing the tip-sample distance to be increased. The comparison between these values and half the one of the fcc unit cell of bulk KCl(001), $6.30/2 = 3.15$ Å, suggests that the structure of 2 ML and 3 ML KCl/Au(111) is quite similar to the one of the bulk crystal.

To confirm this hypothesis and to establish the epitaxy of the KCl islands relative to the Au(111) substrate, we present in Fig. 3 a set of atomically resolved images both on Au(111) and 1 ML and 2 ML KCl. Figure 3(a) shows a large area where the first three KCl layers coexist. Atomic resolution is achieved on each of them. We can observe an occasional contrast inversion on the third layer (black arrow), and temporary loss of resolution on subsequent scan lines demonstrating a large reactivity of the tip. This may either be due to the functionalization of the tip by a KCl cluster, or to a cluster dragged by the tip while scanning, which changes the sensitivity of the apex to anionic and cationic species, respectively. This functionalization is at the origin of the atomic-scale resolution reported in Fig. 3(b), where one kind of atomic species (K^+ or Cl^-) of the second layer is observed. Interatomic distances along the direction of nearest bright spots is (4.5 ± 0.1) Å and (6.2 ± 0.1) Å at 45° from this direction. It is stressed here that in the following, we will refer our crystallographic directions with respect to the KCl primitive unit cell, as depicted in Fig. 3(b) [$\|\mathbf{a}_{\text{KCl}}\| = \|\mathbf{b}_{\text{KCl}}\| = 4.45$ Å, $(\mathbf{a}_{\text{KCl}}, \mathbf{b}_{\text{KCl}}) = 90^\circ$]. The former measurements perfectly correspond to the KCl(001) bulk structure along the $\langle 100 \rangle_{\text{KCl}}$ and $\langle 110 \rangle_{\text{KCl}}$ directions, respectively, and we thus conclude that KCl islands are also (001) terminated. This result is confirmed in Fig. 3(c), where the transition from 1 ML to 2 ML KCl is atomically resolved. The red line highlights the expected one-atom mismatch between the first and the second monolayer along the $\langle 0\bar{1}0 \rangle_{\text{KCl}}$ direction. At last, the atomic resolution of the 1 ML KCl layer along with the trace of the Au(111) reconstruction that is evidenced in the STM contrast (set of red arrows), seems to indicate that the KCl adlayers are aligned along the $\langle 11\bar{2} \rangle_{\text{Au}}$ and $\langle 1\bar{1}0 \rangle_{\text{Au}}$ crystallographic directions of the metallic substrate.

The 2 ML KCl/Au(111) epitaxial relationship was investigated more in detail on the same sample at liquid-helium temperature (4.8 K, cf. Fig. 4). The atomic resolution was recorded on a bare Au(111) area first, then on various 2 ML KCl islands separated by several tens of micrometers from each other [cf. Figs. 4(b) and 4(c)]. It is found that these islands are 30° rotated from each other. Although atomic resolution was not achieved simultaneously on those islands, the extremely low thermal drift of our instrument [95] allows us to compare their crystallographic directions. To gain further resolution, the autocorrelation of the images is used. Figure 4(a) shows the autocorrelation of an STM image of the atomic lattice of Au(111) (raw image shown in inset). Red and green lines show the $\langle 11\bar{2} \rangle_{\text{Au}}$ and $\langle 1\bar{1}0 \rangle_{\text{Au}}$ crystallographic directions (and equivalent directions), respectively. It is thus possible to identify their alignment with the $\langle 100 \rangle_{\text{KCl}}$ and $\langle 010 \rangle_{\text{KCl}}$ crystallographic directions [cf. Figs. 4(b) and 4(c), respectively].

Our results unambiguously prove that from 2 ML and above, the growth of KCl/Au(111) form islands whose in-plane structure is similar to the one of KCl(001). In particular, no buckling of the adlayer was evidenced. The $\langle 100 \rangle_{\text{KCl}}$ and $\langle 010 \rangle_{\text{KCl}}$ directions are aligned along the $\langle 1\bar{1}0 \rangle_{\text{Au}}$ and $\langle 11\bar{2} \rangle_{\text{Au}}$ directions. This leads to three 60° -rotated equivalent epitaxial domain variants, as illustrated in Fig. 4(d). The origin of this peculiar epitaxy has not been investigated and it was neither further quantified as no obvious coincidence relationship

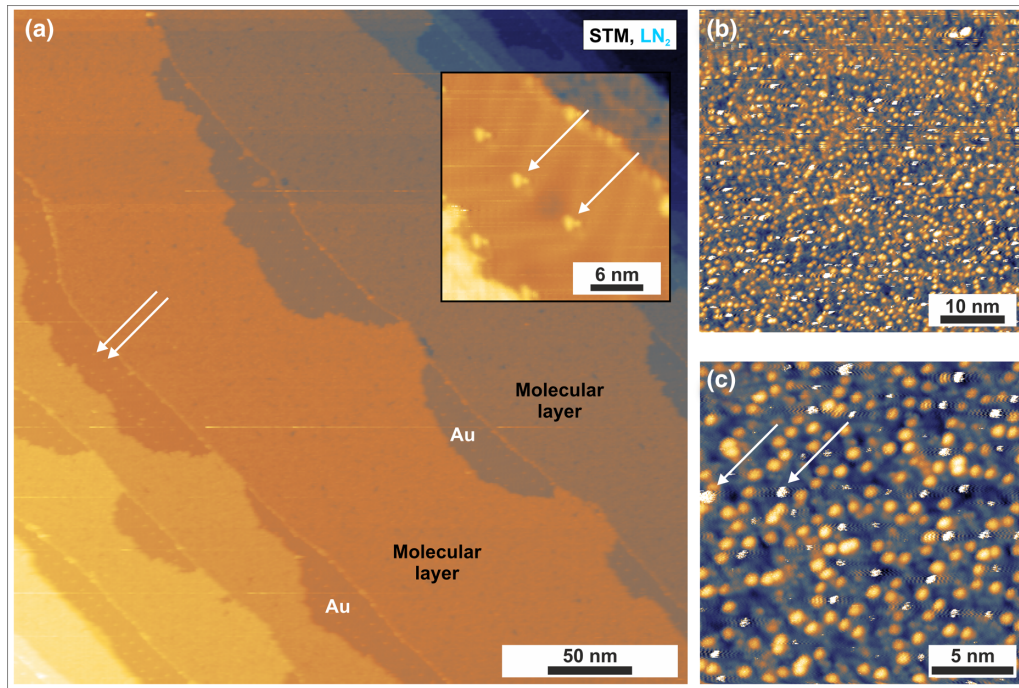


FIG. 5. STM image of the molecular layer on the Au(111) surface at 78 K. (a) Overview of the two-dimensional growth of the layer ($400 \text{ nm} \times 400 \text{ nm}$). White arrows indicate the decoration of the Au(111) elbowed reconstruction by molecules (cf. inset as well). $I_t = 50 \text{ pA}$, $V_b = 2.5 \text{ V}$. (b) STM image of the molecular layer showing an apparent structural disorder. $I_t = 4 \text{ pA}$, $V_b = 2 \text{ V}$. (c) STM image confirming the disordered structure of the molecular layer. White arrows indicate a tip-induced motion of a molecule, or part of a molecule. $I_t = 4 \text{ pA}$, $V_b = 2 \text{ V}$.

between the substrate and the KCl adlayer could easily be put in evidence. We therefore conclude that the structural relation of the (001)-oriented KCl film with respect to the Au(111) surface is incommensurate, but that an *aligned growth mode* takes place, though. This epitaxy might be favored by the small mismatch between Cl^- interatomic distances along the $\langle 100 \rangle_{\text{KCl}}$ direction (4.45 \AA) and the gold interatomic distances along the $\langle 11\bar{2} \rangle_{\text{Au}}$ direction (4.76 \AA). Very similar findings were reported for KCl ultrathin films adsorbed on Ag(100) [41] and on Si(100)- 2×1 [47], an otherwise more reactive surface than Au(111).

B. Curc-di(CN) molecules on Au(111) and 2 ML KCl/Au(111)

1. Structure of the molecular assembly on Au(111)

The morphology of the Curc-di(CN) molecules after thermoevaporation on the bare Au(111) substrate is reported in Fig. 5. Figure 5(a) shows a large-scale image ($400 \times 400 \text{ nm}^2$). The growth of the molecular layer takes place from the step edges with the form of a two-dimensional solid decorating the elbows of the Au reconstruction and the top of the step edges [cf. white arrows in Fig. 5(a) and corresponding inset]. From STM scan lines, a mean molecular height of $(2.3 \pm 0.2) \text{ \AA}$ was measured on this large-scale image. However, peak-to-peak corrugation measured on smaller-scale image gives $\approx 125 \text{ pm}$ [cf. Fig. 5(b)]. This prevents from determining any obvious adsorption geometry of the molecules.

Despite several attempts to increase the resolution of the images, it was impossible to resolve individual molecules within the molecular assembly which looks disordered,

without periodic structure [cf. Fig. 5(c)]. Furthermore, the molecules are mobile under the tip, as evidenced by the large noise level of the tunnel current [cf. white arrows in Fig. 5(c)].

2. Structure of the molecular assembly on 2ML KCl/Au(111)

Figure 6(a) shows a typical distribution of molecular layers formed on 2 ML and 3 ML KCl/Au(111). For this molecular coverage, KCl areas are partially covered by molecules, as shown in the figure where large areas of bare KCl remain visible. Atomic resolution has been achieved on these areas in order to confirm the KCl termination of the surface. The molecules self-assemble into supramolecular islands with a square-shaped morphology. Most of the time, the islands are limited by unidentified adsorbates [cf. white arrows in Fig. 6(b)]. The islands exhibit periodic structures which are identified as molecular rows having two perpendicular orientations [cf. red line in Figs. 6(a) and 6(b)]. This feature recurs on other KCl domain variants, which points towards an epitaxial relationship between the molecular rows and the KCl layer. Height profiles indicate an apparent height of the molecules of $(2.5 \pm 0.1) \text{ \AA}$, which is compatible with a partially flat-lying adsorption configuration of the molecules on the 2 ML KCl.

On the contrary to what was observed on the bare Au(111) substrate, the growth of the first molecular layer on 2 ML KCl/Au(111) shows a remarkable structural organization. Alkali halide surfaces are known to be weakly reactive compared to noble metals such as Au, though. Most of the time, it is found that molecular films form dense and ordered assemblies on metals, and not on ionic crystals.

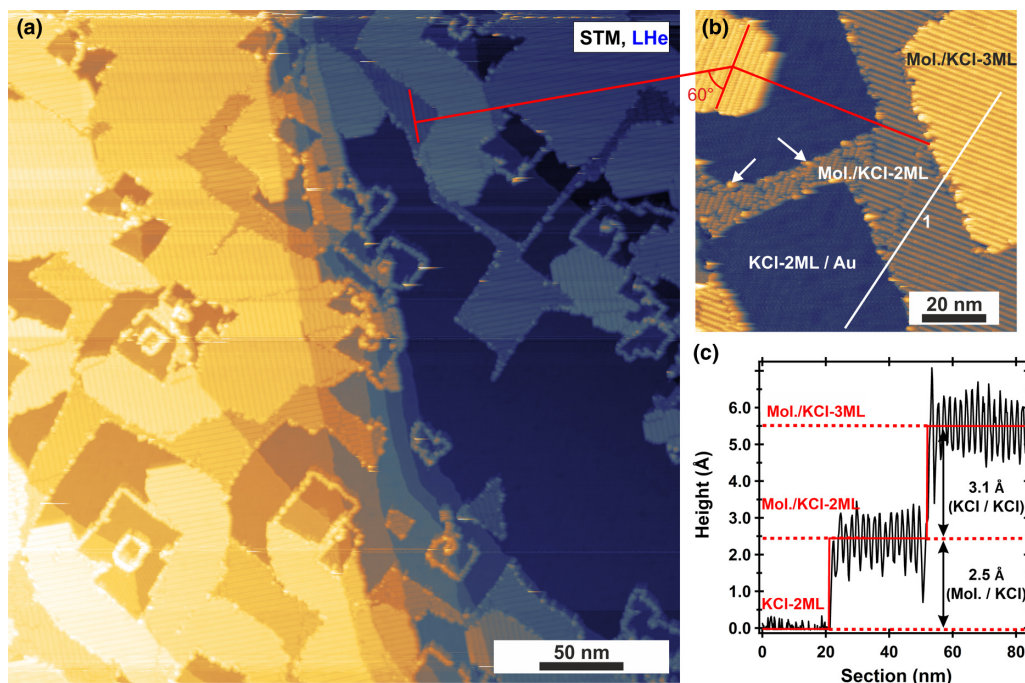


FIG. 6. STM images and profile analysis of Curc-di(CN) molecular layers on the KCl/Au(111) surface acquired at 4.8 K. (a) Overview of the molecular layer partially covering the KCl/Au(111) surface ($400 \text{ nm} \times 400 \text{ nm}$). The molecules form parallel rows on the KCl islands. Some of them are 90° rotated from each other (red line), consistently with the KCl symmetry. $I_t = 5 \text{ pA}$, $V_b = 2.5 \text{ V}$. (b) STM image of molecular rows on 2 ML KCl and 3 ML KCl. $I_t = 700 \text{ fA}$, $V_b = 2.7 \text{ V}$ ($100 \text{ nm} \times 100 \text{ nm}$). (c) Height profile extracted along the white line 1 shown in (b).

3. High-resolution imaging of molecular assemblies

We report in Fig. 7 STM images of the assembly of Curc-di(CN) molecules on 2 ML KCl/Au(111) wherein individual molecules are well resolved. Figure 7(a) shows that the molecular rows are not equivalent. The STM contrast between two adjacent rows [labeled row 1 and row 2 in Fig. 7(a)] is different, whereas it is identical every second row. When going from row 2 to row 1 from left to right, the borders between rows present a darker contrast than when going from row 1

to row 2. Considering that the mean width of the rows is consistent with the dimension of the long axis of a single molecule [$\approx 1.9 \text{ nm}$, cf. Fig. 1(d)], we assume that both rows are one molecule wide. Consequently, the different type of contrast between rows 1 and 2 traces two inequivalent adsorption sites for the molecules and/or two inequivalent molecular adsorption configurations. We will thus no longer characterize the molecular assemblies in terms of “rows,” but rather in terms of “ribbons” consisting of two nonequivalent rows

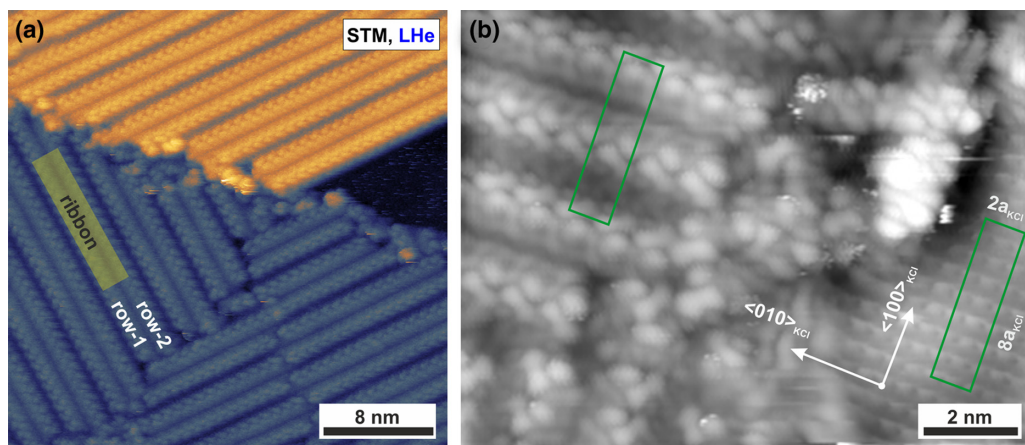


FIG. 7. STM images of the supramolecular phase of the Curc-di(CN) molecules adsorbed on 2 ML KCl/Au(111) acquired at 4.8 K. (a) STM image displaying molecular ribbons consisting of two rows of molecules ($32 \text{ nm} \times 32 \text{ nm}$). $I_t = 10 \text{ pA}$, $V_b = 2.3 \text{ V}$. (b) STM image of a border of a molecular domain with atomic resolution on KCl. The (8×2) molecular supercell is highlighted in green. $I_t = 50 \text{ pA}$, $V_b = 2.3 \text{ V}$.

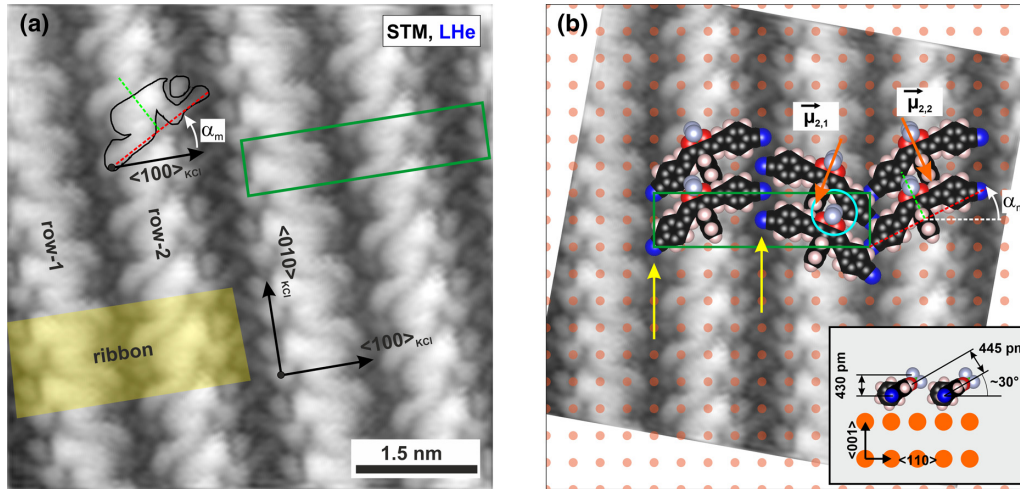


FIG. 8. STM images of the supramolecular phase of the Curc-di(CN) molecules adsorbed on 2 ML KCl/Au(111) acquired at 4.8 K. (a) High-resolution STM image showing two molecular ribbons. The shape defined by the black contour is attributed to a single molecule. The 8×2 supercell has been overlaid in green and the KCl crystallographic axes are indicated. $I_t = 4$ pA, $V_b = 1.77$ V. (b) Sketch of the molecular phase derived with the isomer 2 overlaid on the image shown in (a). The experimental image has been tilted to have the $\langle 010 \rangle_{\text{KCl}}$ axis vertical for readability. The dots depict the K^+ sites acting as anchoring points for the CN groups of the molecules (yellow arrows). For that configuration to be possible, (i) a vertical tilt of the molecules is mandatory (lower inset), which allows for both the compaction of the structure (hence the 8×2 supercell) and the development of favorable $\text{BF}_2\text{-Ph}$ intermolecular interactions (cyan circle) and (ii) a partial relaxation of the tecton to finely accommodate all the interactions along the small groove is mandatory. Here, the vertical tilt angle is 30° , resulting in a structural height of about 430 pm. The dipole moments of the molecules (isomer 2, μ_2) forming the two-molecules pattern per unit cell are indicated as well ($\mu_{2,1}$, $\mu_{2,2}$). Owing to the orientations of the molecules within the unit cell, the resulting dipole $\mu = \mu_{2,1} + \mu_{2,2}$ is aligned with the $\langle 010 \rangle_{\text{KCl}}$ direction, which is polar.

[cf. illustration in Fig. 7(a)]. In this framework, two adjacent molecules form a pattern, whose periodicity accounts for the ribbons periodicity.

Figure 7(b) shows an STM image obtained at the border between 2 ML KCl/Au(111) and a molecular domain. A polynomial plane has been subtracted from this image to enhance the KCl contrast and to reveal the ionic positions, which allows us to deduce the epitaxial relationship between the KCl substrate and the molecules. The molecular ribbons are aligned along the $\langle 010 \rangle_{\text{KCl}}$ direction. The distance between two equivalent rows is (3.57 ± 0.01) nm = $8.02a_{\text{KCl}}$ and the distance between two identical periodic features within a row is (910 ± 10) pm = $2.04a_{\text{KCl}}$. Several other STM images recorded at the border between the KCl substrate and a molecular domain exhibit this (8×2) structure as well. These results point towards a (8×2) point on point epitaxial relationship between the molecular unit cell and the $\text{KCl}(001)$ unit cell [cf. green rectangle in Fig. 7(b)].

The internal structure of the molecular rows is now discussed. Because the width of the tunneling barrier is particularly large in our case (vacuum + 1 ML molecules + 2 ML KCl), relatively large bias voltages (≥ 2 V) are necessary to obtain a detectable tunneling current. These specific imaging conditions scramble the structural information at the intramolecular scale and enhance the contribution of the molecular local density of states (LDOS). Indeed, a molecular electronic state starting around 2.2 eV was put in evidence during $I(V)$ spectroscopy measurements (data not shown). But, at lower bias voltage (1.77 V), i.e., below the electronic state of the molecule, the electronic contribution to the contrast is decreased, which allows us to determine the po-

sition and orientation of individual molecules within a row while getting rid of the LDOS contribution. Figure 8(a) displays two molecular ribbons with intramolecular contrast. Along the row 2, a periodic, asymmetric shape is identifiable, whose borders are highlighted in black. Its dimensions are $\simeq 2$ nm along the long axis (green) which is oriented with an angle $\alpha_m \lesssim 30^\circ$ with respect to the $\langle 100 \rangle_{\text{KCl}}$ direction, and $\simeq 0.9$ nm along the short axis (red). These values make this shape compatible with a single molecule. In the row 1, a similar shape is identifiable too, that can be derived from its counterpart in the row 2 by two subsequent operations: (i) a mirror symmetry with respect to the axis separating the rows [cf. Fig. 8(b)] and (ii) an a_{KCl} shift along the $\langle 010 \rangle_{\text{KCl}}$ direction. Because those shapes repeat periodically over the entire image and that their dimensions match that of individual molecules, we assume that they do correspond to single molecules.

These observations allow us to propose a structural model for the adsorption of Curc-di(CN) molecules on 2 ML KCl/Au(111), namely, the following:

(1) A supramolecular phase (index “ m ” hereafter) defined by a supercell including a two-molecules pattern, whose epitaxy matrix with respect to the primitive $\text{KCl}(001)$ unit cell is $\begin{pmatrix} \mathbf{a}_m \\ \mathbf{b}_m \end{pmatrix} = \begin{pmatrix} 8 & 0 \\ 0 & 2 \end{pmatrix} \begin{pmatrix} \mathbf{a}_{\text{KCl}} \\ \mathbf{b}_{\text{KCl}} \end{pmatrix}$.

Hence, a molecular surface density of $\simeq 0.158$ molecule/nm².

(2) An $\alpha_m \lesssim 30^\circ$ -rotated orientation of the long molecular axis with respect to the $\langle 100 \rangle_{\text{KCl}}$ direction.

(3) The application of a mirror symmetry plus an \mathbf{a}_{KCl} shift to obtain the second molecule of the supercell.

Thus, a structural model for the molecular ribbons can be derived, where the remaining uncertainties are (i) the precise adsorption conformation of the molecule (that we restricted to stereoisomers 1, 2, or 3, however, cf. Fig. 1) and (ii) the precise assignment of the STM contrast to a single molecule with respect to the KCl lattice adsorption site.

The structural model that is proposed is reported in Fig. 8(b) with the isomer 2, which will be justified hereafter. For the sake of the clarity, only one type of ion has been drawn in the figure (K^+ species). Issues (i) and (ii) cannot be unambiguously answered without the help of DFT calculations of the molecular configuration adsorption including the influence of the substrate. These calculations are currently not available. Nevertheless, this model relies on the following assumptions:

(i) The choice of the isomer and its orientation on the substrate plane were thoroughly investigated in order to minimize the molecular sterical hindrance in the model. It turns out that it is easier to make this consistent with the relaxed configuration of the isomer 2, which is slightly more favorable in energy than isomer 1. Isomer 1 is also found to offer less good anchoring sites with respect to the substrate (see item hereafter). As to isomer 3, despite having the most favorable energy configuration, it is too large to avoid unrealistic sterical hindrance. Finally, the strongly asymmetric molecular LDOS contrast seen in STM evokes a nonsymmetric tecton, such as the isomer 2.

(ii) It is likely that the molecule-substrate interaction is steered by the interaction between the CN end groups of the molecule and the K^+ ions [cf. yellow arrows in Fig. 8(b)]. These interactions are known to favor the anchoring of the molecules, as mentioned earlier. Here, the size of the isomer 2 (1.98 nm from N to N) makes this adsorption configuration particularly favorable if the long axis of the molecule is rotated by an angle $\alpha_m = \arctan(2/4) = \pm 26.6^\circ$ with respect to $\langle 100 \rangle_{KCl}$ axis, which fits well the experimental observations. This finding is also compatible with the adsorption configuration of the molecules in rows 1 and 2.

(iii) The specific BF_2 -phenyl intermolecular interaction must play a role in the growth of the supramolecular assembly. More specifically, one envisages an interaction between the fluorine atom, part of the BF_2 group of one molecule, with the π electrons of the phenyl (Ph) groups of the adjacent molecule in the same row. These so-called F- π interactions are known to be attractive, electrostatically driven, and stronger than other halogen- π interactions [96,97]. The distance between two adjacent molecules within a row is too short to envisage the flat adsorption of the molecules without significant sterical hindrance. Therefore, the molecules must partly redress and acquire a vertical tilt angle with respect to the substrate [cf. inset in Fig. 8(b)]. Assuming a molecule whose CN groups remain anchored on the surface, then the conjugated part of the molecule redresses to allow the BF_2 group to develop an optimal attractive interaction with (i) the benzene (Ph) of the ethylenic group and (ii) the meso-Ph group, of the neighboring molecule [cf. cyan circle in Fig. 8(b)]. In the inset of Fig. 8(b), we have chosen a vertical tilt angle of 30° , which brings the B atom of molecule 1 at a distance of $\simeq 445$ pm from the Ph group of the ethylenic group of molecule 2. A slightly shorter distance can be estimated between the B atom of molecule 1 and the meso-Ph of molecule 2. It is difficult to deduce

the distance between the F atom and these Ph groups out of this estimate, but it should be smaller than 445 pm, that is in good agreement with optimum distances reported for F- π interactions ($\simeq 310$ pm, cf. Ref. [96]).

(iv) The fact that the molecules have to tilt vertically favors the compaction of the supramolecular assembly along the rows (in this direction, the molecular packing is maximum as it fits the KCl substrate periodicity), which can partly explain the apparent height of the adlayer observed in STM and in nc-AFM (cf. next section). For instance, a 30° vertical tilt angle yields a structural height of about 430 pm.

(v) To finely accommodate all the interactions, it is likely that the molecules have to relax their conformation a bit further compared to the relaxed configuration of the isolated isomer. This is notably the case for the F- π intermolecular interaction, for which Ph moieties might have to rotate. Nonetheless, the structural model with the relaxed structure of the isomer 2 is yet quite consistent with the experimental observations, which points towards the conclusion that neither the adsorption on the substrate, nor the subsequent supramolecular aggregation, are to drastically modify the conformation of each isolated isomer.

(vi) The dipole moment of isomer 2, $\vec{\mu}_2$, is aligned along the short axis of the molecule [cf. Fig. 1(b)]. In this model, the adsorption configuration of the molecules in the form of a two-molecules pattern per unit cell makes the resulting dipole ($\vec{\mu}_{2,1} + \vec{\mu}_{2,2}$, cf. Fig. 8) aligned along the polar $\langle 100 \rangle$ axis (or equivalently $\langle 010 \rangle$) of the KCl substrate, which must contribute to further stabilize the molecular structure.

(vii) This model can account for the structural origin of the ribbons. Owing to the dimensions of the isomer 2 and to the $\alpha_m = 26.6^\circ$ -rotation angle of its long axis with respect to the $\langle 100 \rangle_{KCl}$ direction, rows 1 and 2 form a structure with a “small groove” (going from row 1 to row 2, from left to right) and a “large groove” (going from row 2 to row 1, from left to right) able to explain the STM contrast, hence the ribbon.

There is therefore a consistent set of site-specific interactions that are steering the growth of the molecular ribbons on the 2 ML KCl/Au(111) substrate and that are likely responsible for their high degree of crystallinity and point-on-point epitaxy with the KCl substrate.

Finally, it should be mentioned that this phase is not the only structure occurring on the 2 ML KCl/Au(111) surface. Some other phases, with different apparent structures, coexist with it. However, this phase represents by far the majority and we infer that the phase polymorphism for these molecules is weak.

C. Curc-di(CN) on KCl(001)

The structural properties of Curc-di(CN) molecules on bulk KCl(001) are now described.

1. Structural characterization by nc-AFM and KPFM

In Fig. 9(a) the adsorption configuration of a $\frac{1}{5}$ ML of Curc-di(CN) molecules on bulk KCl(001) imaged at room temperature is reported. The molecules self-assemble into homogeneous supramolecular domains on the KCl terraces. The domains are well developed, with dimensions of up to 500 nm

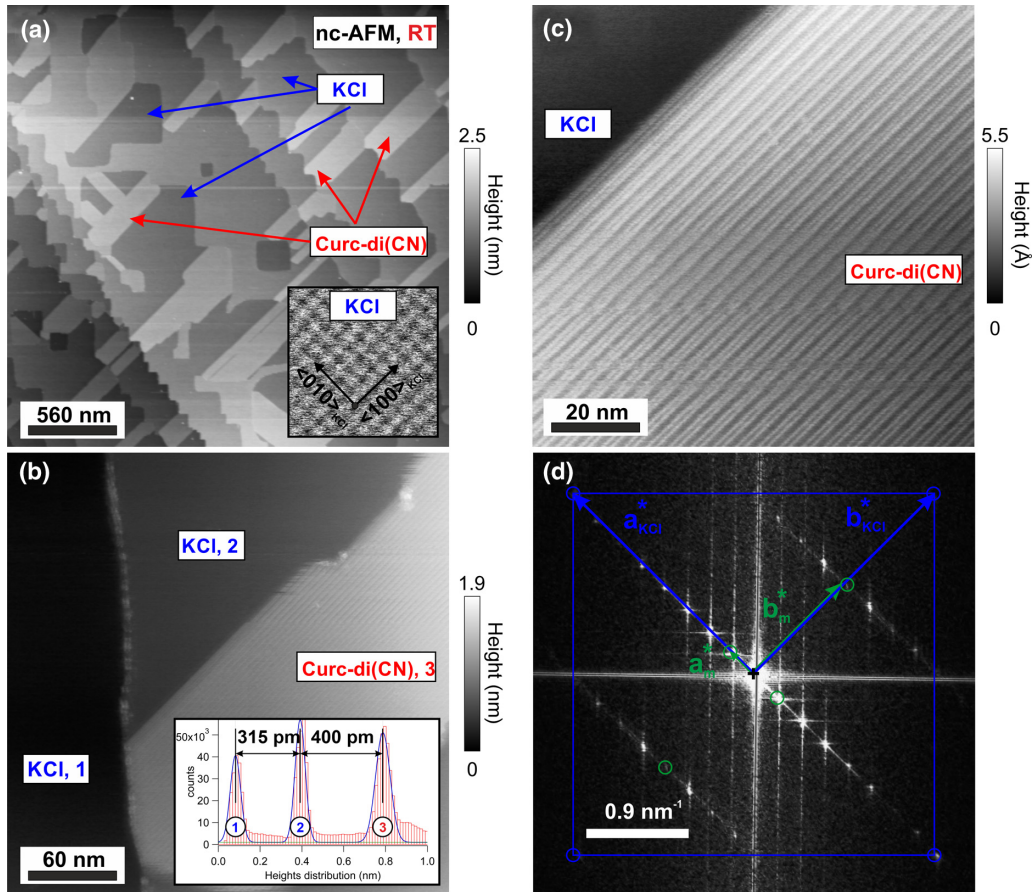


FIG. 9. Curc-di(CN) assemblies on bulk KCl(001), imaged by nc-AFM at room temperature. (a) Large-scale image of Curc-di(CN) ($\approx \frac{1}{5}$ ML) showing the growth of ordered molecular domains between step edges and along the $\langle 100 \rangle_{\text{KCl}}$ direction (cf. atomically resolved image in inset) ($2.8 \mu\text{m} \times 2.8 \mu\text{m}$, $\gamma \approx -5.7 \times 10^{-3} \text{ nN } \sqrt{\text{nm}}$). (b) Zoom on a molecular domain lying on a terrace from a step edge. The histogram in inset gives an estimate of the domain apparent height $\approx 400 \text{ pm}$ ($300 \text{ nm} \times 300 \text{ nm}$, $\gamma \approx -6.8 \times 10^{-3} \text{ nN } \sqrt{\text{nm}}$). (c) Zoom on the molecular domain exhibiting molecular rows whose internal structure gets discernible ($100 \text{ nm} \times 100 \text{ nm}$, $\gamma \approx -8.5 \times 10^{-3} \text{ nN } \sqrt{\text{nm}}$). (d) Fast Fourier transform image (modulus) of image (c). The KCl unit cell ($\mathbf{a}_{\text{KCl}}^*$ and $\mathbf{b}_{\text{KCl}}^*$ vectors) is visible (blue spots and illustrative square) which was not visible in real space. The primitive molecular unit cell (\mathbf{a}_m^* and \mathbf{b}_m^* vectors) is depicted with green spots.

in length, which indicates a large molecular diffusion length on the surface. The domains systematically extend between consecutive step edges. No isolated domain was found on a terrace. This points towards a growth and a nucleation mechanism of the domains starting from the step edges. The aspect ratio of the domains indicates that they grow along the polar $\langle 100 \rangle$ or $\langle 010 \rangle$ crystallographic directions of the surface, as confirmed by the atomic resolution imaging of the substrate [cf. inset in Fig. 9(a)]. Besides, the sharp borders of the domains along the $\langle 110 \rangle$ growth direction suggest both epitaxial order with the substrate as well as internal cohesion of the domain. This is consistent with the anchoring of the CN on the K^+ sites of the substrate reported above. The apparent height of the domains is $(400 \pm 50) \text{ pm}$ [cf. Fig. 9(b)], indicating that the molecules are adsorbed in a nearly flat-lying configuration (cf. discussion hereafter). Therefore, these observations suggest that the molecular growth on bulk KCl corresponds to that found on 2 ML KCl/Au(111).

A detailed investigation of the domains reveals molecular ribbons [cf. Fig. 9(c)]. In Fig. 9(c), simultaneous atomic resolution on KCl [upper part of the frame, barely visible in the real space, but unambiguously visible in the FFT in (d)],

and molecular resolution on the domain (lower part of the frame), allows us to derive a tentative molecular unit cell and its epitaxy with respect to the substrate. The corresponding FFT is shown in Fig. 9(d). The spots of the KCl unit cell are visible (cf. blue square and spots at vertices). The spots of the molecular unit cell are depicted with green circles whose radius stands for our experimental error bars. The molecular unit cells \mathbf{a}_m^* and \mathbf{b}_m^* are sharply aligned with the $\mathbf{a}_{\text{KCl}}^*$ and $\mathbf{b}_{\text{KCl}}^*$ substrate axes. The dimensions of the molecular unit cell in the reciprocal space are $a_m^* = (0.298 \pm 0.115) \text{ nm}^{-1}$, $b_m^* = (1.136 \pm 0.115) \text{ nm}^{-1}$, and $\alpha_m^* = (\widehat{a_m^*, b_m^*}) = 90^\circ$. Hence, dimensions in the real space $a_m = (33.5 \pm 2.6) \text{ \AA}$, $b_m = (8.8 \pm 3.1) \text{ \AA}$, and $\alpha_m = (\widehat{a_m, b_m}) = 90^\circ$. The molecular unit cell is rectangular with its \mathbf{a}_m (\mathbf{b}_m) directions aligned on the \mathbf{a}_{KCl} (\mathbf{b}_{KCl}) substrate axes, i.e., the $\langle 100 \rangle_{\text{KCl}}$ and $\langle 010 \rangle_{\text{KCl}}$ directions. Along the \mathbf{b}_m direction, the molecular unit cell precisely matches 2 KCl unit cells. Along the \mathbf{a}_m direction, the molecular unit cell falls between 7 and 8 KCl unit cells. Owing to our error bars at room temperature, we infer that the structure of the observed molecular ribbons on bulk KCl(001) closely matches that of the ribbons observed on 2 ML KCl/Au(111) by STM.

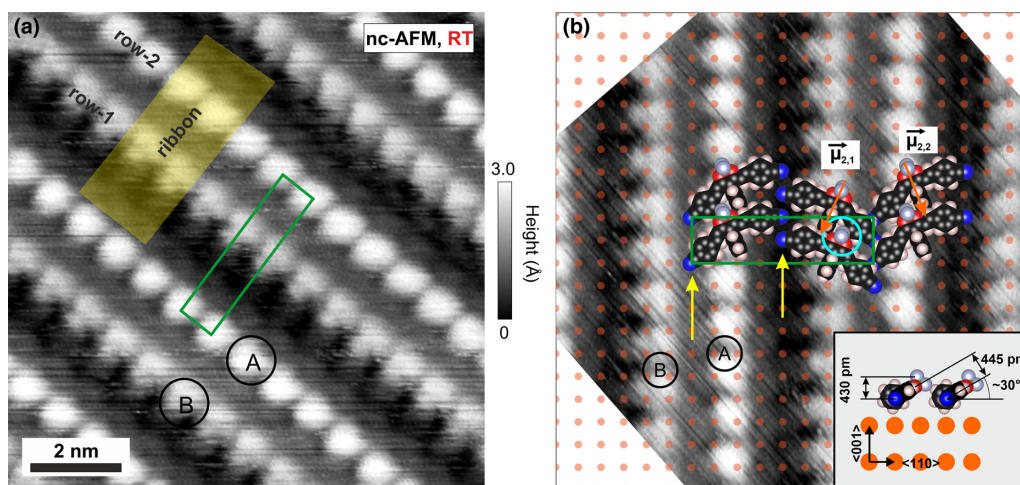


FIG. 10. Supramolecular phase of Curc-di(CN) molecules on bulk KCl(001), imaged by nc-AFM at room temperature. (a) Nc-AFM high-resolution image showing three adjacent molecular ribbons ($10\text{ nm} \times 10\text{ nm}$, $\gamma \simeq -1.1 \times 10^{-2}\text{ nN } \sqrt{\text{nm}}$). Rows 1 and 2 are indicated and the 8×2 supercell is overlaid as well. Type-A and -B features depict two types of molecular contrast tracing two different kinds of molecule-substrate interaction and/or orientation of the molecules. These ribbons have similar features as their counterparts observed by STM on 2 ML KCl/Au(111). (b) Similar illustrative sketch as in Fig. 8. The molecular phase derived with the isomer 2 is superimposed on the image shown in (a). The experimental image has been tilted to have the $\langle 010 \rangle_{\text{KCl}}$ axis vertical for readability. The dots depict the K^+ sites acting as anchoring points for the CN groups of the molecules (yellow arrows). For that configuration to be possible, a vertical tilt of the molecules is mandatory (lower inset), which allows for both the compaction of the structure (hence the 8×2 supercell) and the development of favorable $\text{BF}_2\text{-Ph}$ intermolecular interactions (cyan circle). Here, the vertical tilt angle is also 30° . The model also accounts for types-A and -B features.

To further elucidate the molecular structure in the ribbons on bulk KCl(001), we report in Fig. 10(a), a nc-AFM high-resolution image of three adjacent ribbons. The image contrast exhibits two types of molecular rows (row 1, row 2) whose internal structure is resolved. The molecular unit cell defining the width of the ribbon has been overlaid in green. The contrast along the row 2 exhibits circular bright spots (type-A features) with the periodicity $b_m = (880 \pm 310)\text{ pm}$. The contrast along the row 1 exhibits shapes with similar periodicity, however, with a circular symmetry which is partly lost (type-B features). This traces a locally different interaction with the tip, and hence a two-molecules pattern per unit cell, similarly as what was seen on 2 ML KCl/Au(111). According to their dimensions and periodicity, we assume that these features depict the location of individual molecules, although the contrast cannot be distinctly assigned to any part of a single molecule. When overlaying the structural model derived from the STM results, a good correspondence is found [cf. Fig. 10(b)], which allows us to unambiguously confirm the (8×2) supercell (green rectangle).

We therefore confirm the molecules adsorb on bulk KCl(001) in a point-on-point epitaxy and form a (8×2) supercell similar as the one observed on 2 ML KCl/Au(111). Similar adsorption mechanisms must therefore be at play on both substrates whose reactivities look similar. In particular, the nearly flat-lying adsorption configuration of the molecules is confirmed. The 400-pm apparent height of the molecules derived experimentally [cf. Fig. 9(b)] is consistent with a tilt angle between the surface of the short axis of the molecule of $\leq 30^\circ$ [cf. inset in Fig. 10(b)], yielding a structural height of the molecular structure of $\simeq 430\text{ pm}$.

Typical KPFM images recorded on the molecular ribbons are reported in Fig. 11. The images are featureless. At the

scale of the tip, no major electrostatic contribution can be put in evidence within the ribbons. Row 1 or row 2 are indistinguishable. Topography images recorded simultaneously reveal the molecular structure of the ribbons though, which means that the tip is relatively sharp. We therefore believe that the spatial extension of the electrostatic interaction between the tip and the molecular ribbons has a weak short-range character, in the vertical direction, if any. This seems consistent with the nearly flat-lying adsorption configuration the molecules (and hence of their resulting dipole moment) on the substrate, as discussed above.

D. Optical spectroscopy of Curc-di(CN)

1. Absorption spectra in solvents

Normalized absorption spectra are reported in Fig. 12(a) in the 2.0–3.2 eV range ($\simeq 620\text{--}387\text{ nm}$). The spectra are all measured with well-solubilized molecules and are quite similar. A moderate solvatochromism of $\pm 35\text{ meV}$ ($\pm 5\text{ nm}$) around the absorption maximum of 2.85 eV ($\simeq 437.5\text{ nm}$, acetone) is observed. Considering this and the stability of their shape, the spectra are assumed to be representative of the response of an isolated molecule.

The spectra exhibit a large absorption band which displays two peaks and a less-structured, broader, shoulder above 3 eV. We discuss those transitions in the case of the absorption spectrum obtained in DCM [cf. Fig. 12(b)]. Within the 2.0–3.2 eV energy window, the spectrum was fitted by means of four Gaussian functions to extract the energy, width, and magnitude of the corresponding peaks. Other trial functions (Lorentzian and Voigt functions) were used, but with less good fitting quality, surprisingly. Pseudo-Voigt functions were not tested. Nevertheless, it is not a matter here to detail the

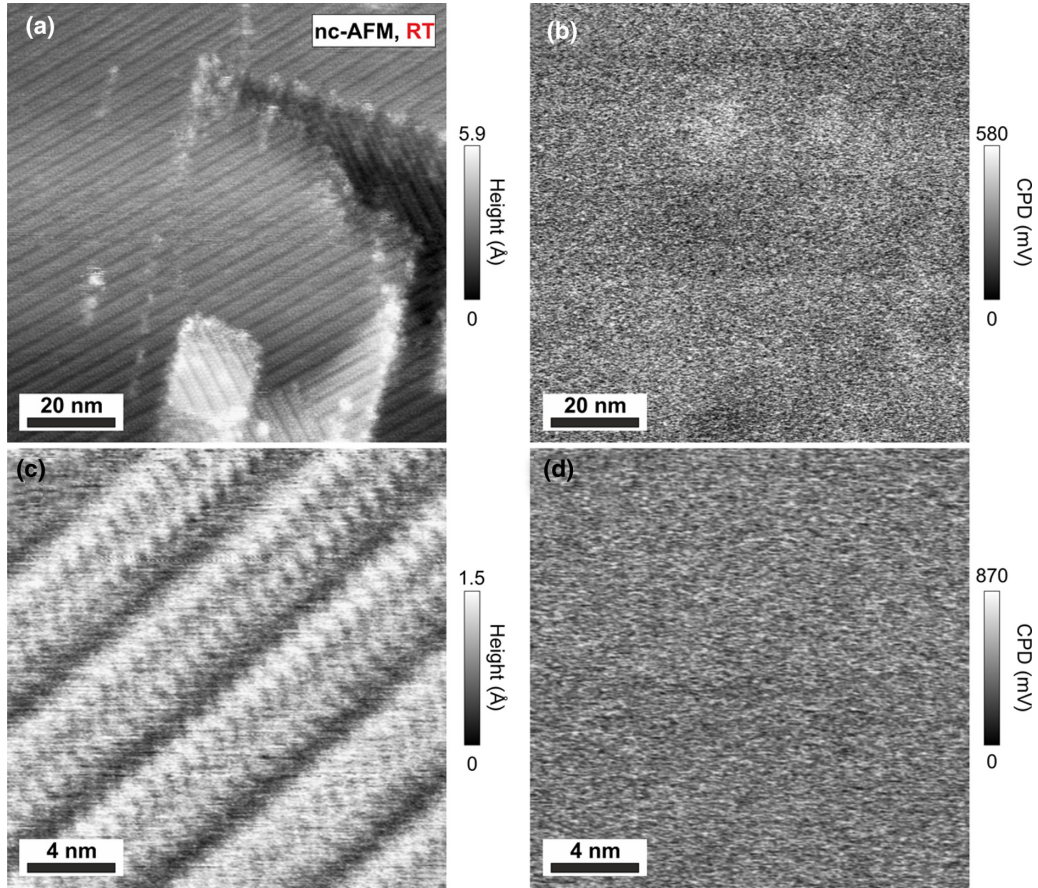


FIG. 11. Nc-AFM and CPD images of Curc-di(CN) molecules on bulk KCl(001) acquired at room temperature. (a), (b) Regular topography and CPD images acquired simultaneously, respectively (100 nm \times 100 nm, $\gamma \simeq -2.3 \times 10^{-2}$ nN $\sqrt{\text{nm}}$). The ribbons are well visible in the topography image whereas no contrast can be assigned to them in the CPD channel. (c), (d) Zoom (topography and CPD, respectively) (20 nm \times 20 nm, $\gamma \simeq -2.8 \times 10^{-2}$ nN $\sqrt{\text{nm}}$). Despite getting closer from the molecular structures, no CPD contrast can be revealed.

microscopic structure of the dielectric function that enters in the expression of the absorbance [cf. Eq. (2)]. Our goal was not to fit the spectra to extract $\tilde{\epsilon}(\lambda)$ quantitatively, but rather to establish a rational methodology to estimate the main characteristics of the absorption peaks, and primarily their energy location. With four Gaussian functions, the fit quality is good, with a residual that does not exceed $\pm 1\%$.

The fit parameters (energy, width, and magnitude of the Gaussian functions) for the four transitions are reported in Table I. The first two peaks are estimated to be located at $E_1 = (2.660 \pm 0.027)$ eV [$\lambda_1 = (466.6 \pm 4.7)$ nm] and $E_2 = (2.818 \pm 0.028)$ eV [$\lambda_2 = (440.5 \pm 4.4)$ nm]. The shoulder is properly reproduced by the fit only if two near peaks are considered, whose energies are $E_3 = (2.966 \pm 0.030)$ eV

[$\lambda_3 = (418.5 \pm 4.2)$ nm] and $E_4 = (3.009 \pm 0.030)$ eV [$\lambda_4 = (412.5 \pm 4.1)$ nm]. It is thus noticed that $E_2 - E_1 \simeq E_3 - E_2 \simeq 155$ meV. The residual of the fit is quite sensitive to the fit parameters. For instance, a mere 5-meV shift in the location of a peak is easily identifiable. The relative error bars of our fit parameters are therefore set to 1% for the energy and 5% for the width and the magnitude of the Gaussian functions, but are hence overestimated.

The peak No. 1 has a slightly larger magnitude ($\simeq 0.61$) than the peak No. 2 ($\simeq 0.60$). The peak No. 3 has a weaker magnitude ($\simeq 0.21$) compared to peaks Nos. 1 and 2. In absorption spectroscopy, the magnitude of an absorption peak relates to the oscillator strength for the corresponding transition, proportional to the transition dipole moment $\vec{\mu}_t$ of

TABLE I. Table of the fit parameters of the absorption peaks of Curc-di(CN) molecules in DCM.

Label "x"	Transition	λ (nm)	Energy (eV)	$(E_x - E_1)$ (meV)	Gaussian width (meV)	Mag. (a.u.)
4	$\{S_0 \rightarrow S_{ij}\}$	(412.5 ± 4.1)	(3.009 ± 0.030)	(349 ± 7)	(303 ± 15)	(0.515 ± 0.026)
3	$S_{00} \rightarrow S_{12}$	(418.5 ± 4.2)	(2.966 ± 0.030)	(306 ± 6)	(95 ± 5)	(0.207 ± 0.010)
2	$S_{00} \rightarrow S_{11}$	(440.5 ± 4.4)	(2.818 ± 0.028)	(158 ± 4)	(96 ± 5)	(0.595 ± 0.030)
1	$S_{00} \rightarrow S_{10}$	(466.6 ± 4.7)	(2.660 ± 0.027)	0	(92 ± 5)	(0.607 ± 0.031)

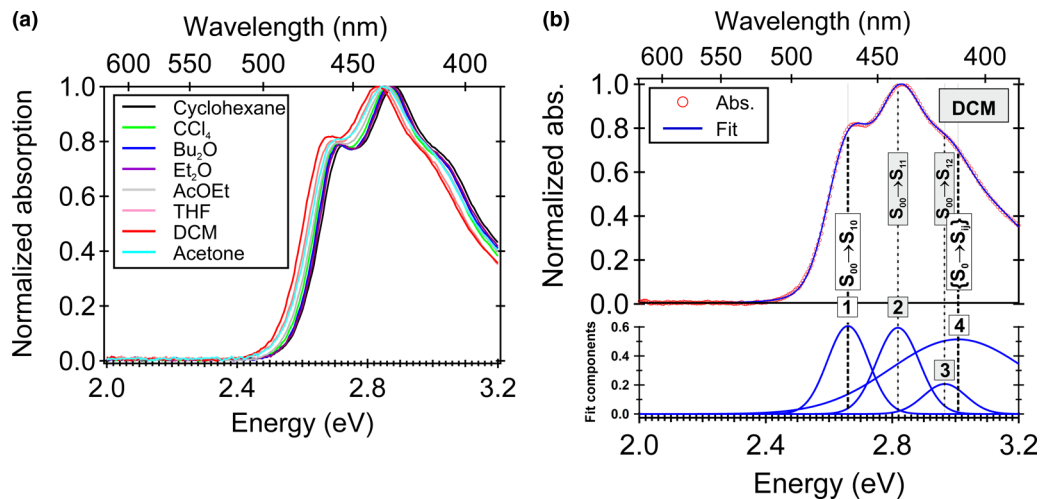


FIG. 12. (a) Normalized absorption spectra of Curc-di(CN) in various solvents. (b) Normalized absorption spectrum of Curc-di(CN) in DCM and corresponding fit with four transitions. The first three are tracing a π - π^* transition ($S_{00} \rightarrow S_{10}$) and vibronic replicas ($S_{00} \rightarrow S_{11}$ and $S_{00} \rightarrow S_{12}$). The fourth, broad, one labeled $\{S_0 \rightarrow S_{ij}\}$ is ascribed to a set of transitions whose detailed structure is not resolved, from the S_0 electronic ground state to S_{ij} states, where $i > 1$ and $j \geq 0$ (cf. text and Table I for details).

the molecule, which must not be confused with its permanent dipole moment $\vec{\mu}$. Therefore, the absorption spectra suggest that the transition dipole moments for peaks Nos. 1 and 2 are quite similar and the most prominent of the absorption process. The peak No. 3 is located $\simeq 40$ meV below the peak No. 4 whose magnitude is comparatively more intense ($\simeq 0.52$), but however comparable to those of peaks Nos. 1 or 2. The widths of peaks Nos. 1, 2, and 3 are similar ($\simeq 94$ meV), but the width of peak No. 4 is three times broader.

Because the peaks Nos. 1, 2, and 3 are energetically equidistant ($\simeq 155$ meV) and have similar widths ($\simeq 94$ meV), we interpret them as the trace of a local π - π^* excited state ($S_0 \rightarrow S_1$ transition), including a vibronic progression. Introducing double indices for the singlets S_{ij} , where i stands for the electronic singlet state ($i = 0$ or 1) and j for the vibronic state in the S_1 state ($j = 0, 1, 2, \dots$), E_1 , E_2 , and E_3 depict the energies of the transitions $S_{00} \rightarrow S_{10}$, $S_{00} \rightarrow S_{11}$, and $S_{00} \rightarrow S_{12}$, respectively [cf. Fig. 12(b)]. As to the peak No. 4, its features, among which its broadness, cannot be put in relation with the former vibronic progression. Therefore, we do not ascribe it to a single transition and assume that it rather features a set of several energetically close transitions from the S_0 electronic ground state to S_{ij} states, where $i > 1$ and $j \geq 0$. We label this peak as $\{S_0 \rightarrow S_{ij}\}$ in Table I and in Fig. 12, where the brackets symbolize the set of transitions. Those trends (energy location of the $S_0 \rightarrow S_1$ transition, magnitudes of the peaks within the vibronic progression, energy proximity of transitions above the $S_0 \rightarrow S_1$ one) are found to be in good agreement with the spectroscopic properties of others curcuminoid derivatives in solvent [75,98].

2. DRS on KCl(001)

The DR spectra of the molecules on KCl(001) for coverages ranging from 0 to $\simeq 3$ ML, as calibrated by nc-AFM imaging, are reported in Figs. 13(a) and 13(b). The molecules absorb in a band spanning from 2.4 up to 3.2 eV (limit of detection), much like in solvent. The structure of the band is

well resolved from the sub-ML regime [cf. Fig. 13(a)], up to the multilayer regime [cf. Fig. 13(b)].

In the early stages of growth, the spectra are yet structured. From 1 to 3 ML, three main transitions are distinguishable, but like in the case in solvent, four are to be considered for fitting the spectra. The fit process is performed out of the following assumption. Because the molecular adlayer thickness is much smaller than the illumination wavelengths and that a single molecular phase was mainly observed on the surface, it is inferred that the fitting DRS functional has the same form as the optical density in solvent [cf. Eq. (2)], which was restricted to a simple set of Gaussian functions, as described in the section above. Although the choice of Gaussian functions is not optimal to fit the DR spectra [60], this approach makes the DRS/absorption in solvent benchmarking self-consistent. Therefore, the DR spectra have been fitted accordingly [cf. Fig. 13(d)] and the fit parameters (locations, magnitudes, and widths) are reported in Table II. Here again, the fit quality is good with a residual that does not exceed $\pm 2\%$ (1 ML and 3 ML regime). To make the comparison easier, the absorption spectrum in DCM and its fit components have been reported in Fig. 13(c).

Focusing on the 1 ML regime, the four peaks are located at $E_1 = (2.620 \pm 0.027)$ eV [$\lambda_1 = (473.8 \pm 4.9)$ nm], $E_2 = (2.783 \pm 0.028)$ eV [$\lambda_2 = (446.0 \pm 4.5)$ nm], $E_3 = (2.925 \pm 0.030)$ eV [$\lambda_3 = (424.4 \pm 4.4)$ nm], and $E_4 = (2.929 \pm 0.030)$ eV [$\lambda_4 = (423.8 \pm 4.3)$ nm]. Thus, $E_2 - E_1 \simeq E_3 - E_2 \simeq 160$ meV, which is nearly alike the case in solvent (155 meV). This trend is confirmed with the other parameters, namely, (i) the magnitudes of peaks Nos. 1, 2, and 3 decrease consistently, (ii) the magnitude of the peak No. 4 is comparable, but smaller than that of peak No. 1, and (iii) the widths of peaks Nos. 1, 2, and 3 are close and a bit larger ($\simeq 104$ meV) than those in solvent ($\simeq 94$ meV), whereas the peak No. 4 is three times larger ($\simeq 300$ meV).

Therefore, the 1 ML DR spectra and the absorption spectrum in DCM are quite similar in shape. We therefore assign the DR peaks consistently. The peaks Nos. 1, 2, and 3 are

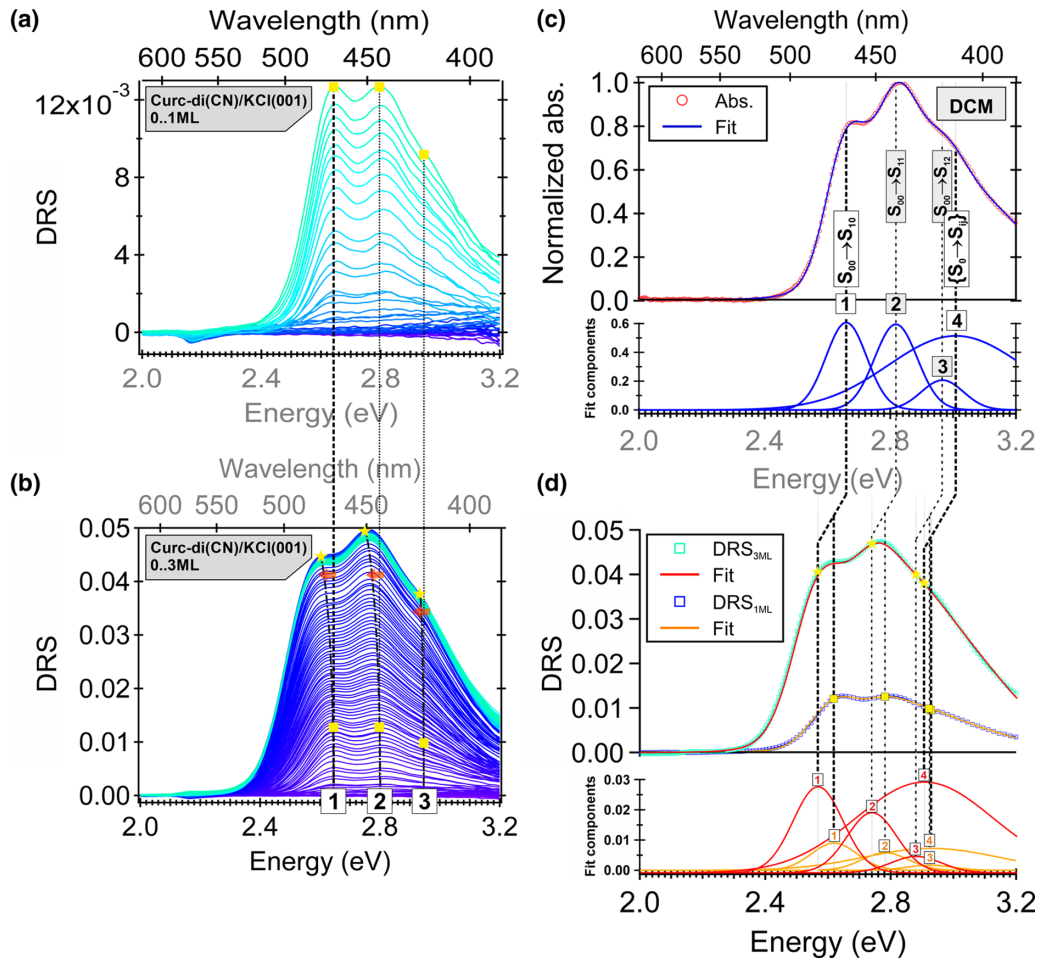


FIG. 13. DR spectra of Curc-di(CN) molecules adsorbed on KCl(001). (a) 0 to 1 ML regime. Three peaks are identified (squares), but four are required to perform the fit(cf. (d)). (b) 0 to 3 ML regime. One has reported the squares to stress the 1 ML case. Up to 3 ML, the peaks remain visible (stars) and are slightly redshifted (cf. text for details). (c) Normalized absorption spectrum of Curc-di(CN) in DCM [similar to Fig. 12(b)] and corresponding fit. (d) DR spectra for 1 ML (dark blue) and 3 ML (turquoise) and corresponding fits (orange and red lines, respectively) including four transitions which are ascribed to the $S_{00} \rightarrow S_{1j}$ (with $j = 0, 1, \text{ and } 2$) and $S_{00} \rightarrow S_{20}$ transitions. From solvent to 1 ML/KCl, a slight redshift of the peaks is noticed, increasing up to 3 ML (cf. text and Table II for details).

ascribed to the $S_{00} \rightarrow S_{1j}$ (with $j = 0, 1, \text{ and } 2$) vibronic progression. The peak No. 4 is ascribed to a set of unassigned transitions labeled as $\{S_0 \rightarrow S_{ij}\}$, where $i > 1$ and $j \geq 0$. The main discrepancy between the DR peaks and the peaks in solvent stems from their redshift. For the three peaks forming the $S_{00} \rightarrow S_{1j}$ transition (with $j = 0, 1, \text{ and } 2$), the shift

from solvent to 1 ML/KCl(001) is similar for each peak and reaches $\simeq -40$ meV. For the $\{S_0 \rightarrow S_{ij}\}$ transition (with $i > 1$ and $j \geq 0$), the resulting shift from solvent to 1 ML/KCl(001) is more pronounced ($\simeq -80$ meV).

In the 3 ML regime, the former peaks are further redshifted. All the peaks forming the $S_{00} \rightarrow S_{1j}$ transition (with $j = 0, 1,$

TABLE II. Table of the fit parameters of the DR spectra peaks of Curc-di(CN) molecules on KCl(001) (1 ML and 3 ML regimes).

Label "x"	regime	λ (nm)	Energy (eV)	$(E_x - E_1)$ (meV)	$(E_x - E_{x,\text{abs.}})$ (meV)	Gaussian width (meV)	Mag. $\times 10^{-3}$ (a.u.)
4	1 ML	(423.8 ± 4.3)	(2.929 ± 0.030)	(309 ± 6)	(-80 ± 2)	(300 ± 15)	(7.3 ± 0.4)
	3 ML	(427.4 ± 4.4)	(2.904 ± 0.030)	(339 ± 7)	(-105 ± 2)	(308 ± 15)	(30.5 ± 1.6)
3	1 ML	(424.4 ± 4.4)	(2.925 ± 0.030)	(305 ± 6)	(-41 ± 1)	(103 ± 5)	(1.7 ± 0.1)
	3 ML	(431.3 ± 4.5)	(2.878 ± 0.029)	(313 ± 7)	(-88 ± 2)	(114 ± 6)	(5.5 ± 0.3)
2	1 ML	(446.0 ± 4.5)	(2.783 ± 0.028)	(163 ± 3)	(-35 ± 1)	(105 ± 5)	(5.8 ± 0.3)
	3 ML	(453.5 ± 4.6)	(2.737 ± 0.030)	(172 ± 3)	(-81 ± 2)	(112 ± 6)	(20.2 ± 1.0)
1	1 ML	(473.8 ± 4.9)	(2.620 ± 0.027)	0	(-40 ± 1)	(103 ± 5)	(9.0 ± 0.5)
	3 ML	(483.9 ± 5.1)	(2.565 ± 0.027)	0	(-95 ± 2)	(112 ± 6)	(28.9 ± 1.4)

and 2) are shifted by an equivalent quantity of $\simeq -50$ meV (cf. Table II). The $\{S_0 \rightarrow S_{ij}\}$ transition (with $i > 1$ and $j \geq 0$) exhibits a different behavior and is shifted by $\simeq -25$ meV only. The other fit parameters keep similar trends otherwise.

Possible origins of the inequivalent redshift of the $S_{00} \rightarrow S_{1j}$ (with $j = 0, 1$, and 2) and $\{S_0 \rightarrow S_{ij}\}$ (with $i > 1$ and $j \geq 0$) transitions evidenced by the DR spectra for the two situations: solvent \rightarrow 1 ML/KCl(001) and 1 ML/KCl(001) \rightarrow 3 ML/KCl(001), are discussed in Sec. IV.

Finally, let us point out that from 1 to 3 ML, the magnitudes of the peaks of the $S_{00} \rightarrow S_{1j}$ transition (with $j = 0, 1$, and 2) are multiplied by a factor of 3, which is found to be consistent with the linear approach we have used to perform the fits. For the $\{S_0 \rightarrow S_{ij}\}$ transition (with $i > 1$ and $j \geq 0$), this trend is less pronounced. However, the conclusion about the linearity of DRS signal for that transition does not stand, as it results from the superposition of several transitions which are presumably not all shifted consistently.

IV. DISCUSSION

A. Evidence for weak adsorption

On the one hand, the structural analyses show that Curcidi(CN) molecules adsorb in a similar manner on 2 ML KCl/Au(111) and on bulk KCl(001). In the monolayer regime, the molecules form supramolecular ribbons featuring a well-stable thermodynamical phase, as demonstrated by (i) its weak polymorphism, (ii) the large extension of the molecular domains, and (iii) the fact that these are consistently imaged at liquid-helium temperature and at room temperature. The periodic structure of the ribbons is described by an 8×2 supercell wherein the molecules pack into a two-molecules pattern, which can be referred to as a dimer. It is found that, among several possible stereoisomers, it is the isomer 2 which suits the best to the structural model.

On the other hand, the optical analyses show that upon adsorption on the KCl substrate (i) the molecules do not undergo severe conformational changes compared to the situation in solvent, (ii) the aggregation yielding the supramolecular assembly does not significantly modify the optical properties of the individual molecule, and (iii) the size of the light spot being 5 mm in diameter on the substrate, the DR spectra reflect an averaged optical signature of the molecules that features a quite homogeneous structural order all over the substrate, which is consistent with the weak phase polymorphism.

However, no obvious trace of molecular dimerization, that might translate into a significant modification of the DR spectra (1 ML regime) compared to the absorption spectra in solvent is observed. Instead, the spectra all exhibit four absorption peaks identified as a $S_{00} \rightarrow S_{1j}$ (with $j = 0, 1$, and 2) vibronic progression and a set of $\{S_0 \rightarrow S_{ij}\}$ transitions (with $i > 1$ and $j \geq 0$) in the molecule. The adsorption of the molecules on the KCl substrate only induces a redshift of the spectra (bathochromic effect), but does not drastically modify their optical signature.

The influence of the molecular packing on optical absorption and photoluminescence was originally worked out by Kasha for aggregates dominated by intermolecular Coulomb coupling between parallel transition dipole moments of, at

least, two neighboring excited molecules, leading to the classification between J- (bathochromic effect) and H-aggregates (hypsochromic effect) [99,100]. This kind of coupling is naturally favored when planar molecules are stacked into a dimericlike parallel arrangement, often under the influence of π - π stacking, hereby tracing a preaggregation stage: monomer \rightarrow dimer \rightarrow oligomer (if applicable). Correlating the aggregation process to the structure of the optical spectra is the framework of excimers theory, including J- and H-aggregates and their excitonic interactions [99–109] such as long-range Coulomb coupling, vibronic coupling, intermolecular charge transfer, and peculiar packing geometries (linear and bent aggregates, two-dimensional herringbone and “HJ” aggregates, chiral aggregates, ...) [109]. The interplay between these couplings strongly depends on the packing type, which reconfigures the molecular levels and hence the structure of the absorption spectra.

Here, the DR spectra look similar to the absorption of the monomer in solvent and no major excitonic effect is evidenced. Therefore, we infer that the two-molecules pattern seen in the supramolecular assemblies results from a combination of intermolecular and molecule-substrate interactions which are weak and not importantly modified by the occurrence of the transition dipole upon optical absorption.

B. Influence of Coulomb interactions

Because intermolecular Coulomb interactions are known to promote excitonic effects and that no excitonic effect is observed in the DR spectra, it is important to estimate their strength in our system, where they may arise due to the coupling between the molecular dipole moments $\vec{\mu}$. To this end, we performed a numerical estimation of the electrostatic (Coulomb) energy of the molecules in the supramolecular assembly out of a basic system: each molecule is reduced to a two-point charge set ($q_p = +q$, $q_n = -q$), separated by a distance d . At large distance from it, the system behaves as a dipole of strength $\mu = qd$. Sterical hindrance effects between the as-described molecules and the influence of the ionic surface are not accounted for. We then consider a set of $N \times N$ dipoles forming a periodic structure whose unit cell is depicted in Fig. 14(a). The electrostatic energy E_{el} is estimated at the location M of the central dipole in the $N \times N$ assembly. E_{el} is plotted against the angle α that each dipole forms with respect to the horizontal axis [cf. Fig. 14(a), lower left scheme, $\alpha \in [0; 360^\circ]$]. To account for the two-molecules pattern, following the description of the experimental unit cell, we force the angle α' of the internal molecule of the unit cell to be $\alpha' = \pi - \alpha$. The internal molecule is located at distances a_c and b_c from the lower left molecule of the unit cell along a_{KCl} and b_{KCl} axes, respectively [cf. Fig. 14(a)]. The parameters a , b , a_c , b_c , and θ of the simulated unit cell are derived from the experimental unit cell, namely, $a = a_m = 8a_{KCl} = 3.56$ nm, $b = b_m = 2a_{KCl} = 0.89$ nm, $a_c = 0.6a = 2.14$ nm, $b_c = 0.5b = 0.445$ nm, and $\theta = 90^\circ$. We then sum the set of point charges, without dipolar approximation. The electrostatic energy is estimated in M according to

$$E_{dip}(M) = E_n(M) + E_p(M) \quad (3)$$

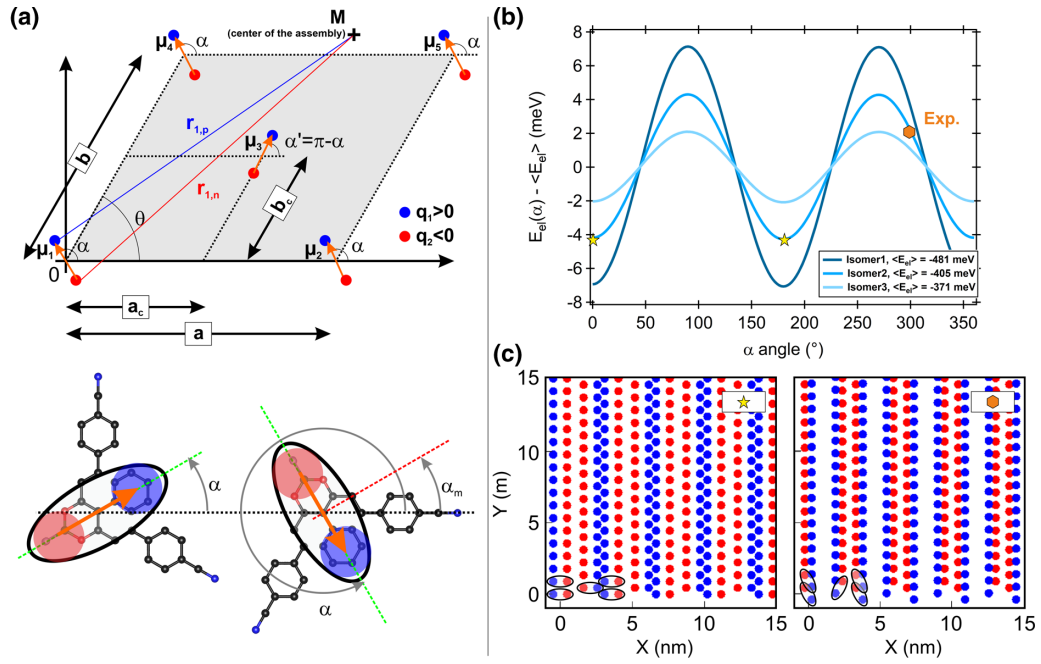


FIG. 14. (a) Upper part: scheme of the unit cell chosen to perform the calculation of the Coulomb energy of the system. Each molecule is depicted as a two-point-charges system forming a dipole μ . The energy is estimated at the point M , located in the center of the molecular assembly. Lower part: illustration of the angle α against which the Coulomb energy is calculated (left) and illustration of the angle α_m , as defined in the experimental unit cell, such that $\alpha = \alpha_m + 270^\circ$ (right). (b) Coulomb energy minus mean energy against α for isomers 1, 2, and 3, of mean energy -481 , -405 , and -371 meV, respectively. For isomer 2, one has stressed the minima obtained for two equivalent configurations $\alpha = 0^\circ$ and $\alpha = 180^\circ$ (stars), as well as the configuration of the experimental unit cell $\alpha_m \simeq 27^\circ$ (orange mark), hence, $\alpha \simeq 300^\circ$. Whatever the isomer, the modulation of the Coulomb energy does not exceed 10 meV. (c) Illustrative sketch of the organization of the dipoles for the minimum Coulomb energy ($\alpha = 0^\circ$ or, equivalently, $\alpha = 180^\circ$, left) and for the experimental case ($\alpha \simeq 300^\circ$, right).

with

$$E_{n,p}(M) = q_{n,p} \sum_{i=1}^{N^2-1} V_{i \rightarrow n,p}(M) \quad (4)$$

and

$$V_{i \rightarrow n,p}(M) = \frac{1}{4\pi\epsilon_0} \frac{q_i}{r_{i \rightarrow n,p}(M)}, \quad (5)$$

where $r_{i \rightarrow n,p}(M)$ is the distance between M and the i th negative (“ n ”) or positive (“ p ”) charge in the assembly. The convergence of the calculations was found to be good for $N \geq 11$. We have set $N = 21$. The calculations were performed for each isomer whose dipole moment and short-axis length were determined by DFT [cf. Fig. 1(a)]. For isomers 1, 2, 3, these quantities are $\mu_1 \simeq 8.4$ D, $\mu_2 \simeq 7.3$ D, $\mu_3 \simeq 6.3$ D and $d_1 \simeq 6.15$ Å, $d_2 \simeq 5.5$ Å, $d_3 \simeq 4.45$ Å, respectively. The corresponding point charges are consequently equal to $q_{p,1} = \mu_1/d_1 = 0.317e$, $q_{p,2} = \mu_2/d_2 = 0.277e$, and $q_{p,3} = \mu_3/d_3 = 0.239e$, e being the elementary charge ($e = 1.6 \times 10^{-19}$ C).

The calculated electrostatic energy is reported in Fig. 14(b) for the three isomers. For ease of reading, instead of $E_{el}(\alpha)$, one has plotted $E_{el}(\alpha) - \langle E_{el} \rangle_\alpha$, where $\langle E_{el} \rangle_\alpha$ is the mean electrostatic energy over the α range. For isomers 1, 2, and 3, one has $\langle E_{el} \rangle_{\alpha,1} = -481$ meV, $\langle E_{el} \rangle_{\alpha,2} = -405$ meV, and $\langle E_{el} \rangle_{\alpha,3} = -371$ meV, respectively. Therefore, the system is logically found to be the most stable with the isomer exhibit-

ing the largest dipole moment. The axis of symmetry seen in the figure with respect to $\alpha = 180^\circ$ stems from the symmetry of the problem. The energy minimum is found for $\alpha = 0^\circ$ [or equivalently 180° , cf. stars for the curve of isomer 2 in Fig. 14(b)] and is found to be located a couple of meV below the mean energy value of each isomer, only. The corresponding charge assembly configuration is reported in Fig. 14(c) (left). The molecules align their charges to form charged rows of alternating signs along the $\langle 010 \rangle_{KCl}$ direction. This structure is not compatible with the experimental one. The electrostatic energy of the experimental unit cell is obtained for $\alpha = 270 + \alpha_m = 300^\circ$ [cf. Fig. 14(a), lower right scheme]. It has been stressed in Fig. 14(b) for the isomer 2 with an orange mark. The corresponding charge assembly configuration is reported in Fig. 14(c) (right), with well-identifiable ribbons. Structurally, this configuration is significantly different compared to the former one. However, their electrostatic energies differ by less than 10 meV only [cf. Fig. 14(b)]. Whatever the isomer, the mean electrostatic energy ($\simeq -400$ meV) suggests that intermolecular Coulomb interactions play a role in the adsorption configuration (vertical interactions) of the molecules. Thus, they potentially favor the alignment of the molecular dipoles along the $\langle 100 \rangle_{KCl}$ polar directions of the substrate. But, considering their very weak modulation with α (in-plane interactions), we conclude that the structure of the unit cell and the two-molecules pattern is inefficient to promote Coulomb coupling able to yield major excitonic effects at room temperature.

C. “Solvent to surface” and “condensed-phase”-induced redshifts

From the situation in solvent to the 1 ML regime on KCl(001), the three absorption peaks forming the $S_{00} \rightarrow S_{1j}$ transition (with $j = 0, 1, 2$) are equivalently redshifted ($\simeq -40$ meV, cf. Table II). But the $\{S_0 \rightarrow S_{ij}\}$ (with $i > 1$ and $j \geq 0$) transition is shifted more ($\simeq -80$ meV), which makes the redshift of the overall absorption band nonrigid compared to the situation in solvent. Therefore, instead of a strong effect of the molecular packing, this observation might rather suggest a conformational change of the molecule upon adsorption, compared to the situation in solvent. However, the relative magnitudes and widths of the peaks remain similar between the situation in solvent and on the surface. Therefore, the conformational change must be moderate. To make this observation consistent with our results, one might propose the following explanation. The activation barrier to switch from an isomer to another one is unknown, but the DFT calculations predict that the most stable isomer is isomer 3. The absorption spectra in solvent might therefore mainly reflect the absorption properties of this particular isomer. On the surface, the isomer 3 is too large to be involved in the observed assemblies. The model fits best with the isomer 2, whose optical absorption is mostly reflected in the DR spectra. Therefore, from the gas phase, the adsorption process selects isomer 2 because of its size and ability to place its CN groups above K^+ sites, which in turn changes the optical signature, as compared to the solvent.

This observation is consistent with the results by Müller *et al.* on PTCDA adsorbed on KCl thin films on Ag(100) [58] who reported that the vibrational modes of the adsorbed molecule are very similar to those of the free molecule, but due to the presence of the substrate additional low-energy modes couple to the transition. This was further confirmed by DFT calculations where the redshift of the first optical excitation was found to stem from both the distortion of the molecule due to the interaction with the surface and the electrostatic potential of the surface play an important role [110].

Regarding the 1 ML \rightarrow 3 ML growth on KCl(001), it is again observed that the three absorption peaks forming the $S_{00} \rightarrow S_{1j}$ transition (with $j = 0, 1, 2$) are equivalently redshifted ($\simeq -50$ meV, cf. Table II), whereas the $\{S_0 \rightarrow S_{ij}\}$ (with $i > 1$ and $j \geq 0$) transition is redshifted too, but to a less extent ($\simeq -25$ meV). Therefore, from 1 ML to 3 ML on KCl(001), the redshift of the transitions is nonrigid either. For the $S_{00} \rightarrow S_{1j}$ transition (with $j = 0, 1, 2$), a similar observation has been reported with bis-pyrene molecules adsorbed on KCl(001) and NaCl(001) [60]. As discussed in this reference, a potential microscopic explanation to the redshift would be the strengthening of gas to solid shift effects [101] due to the stabilization of the excited state in the 3 ML molecular crystal, which stands for a condensed phase [111]. This is particularly true if one assumes the layers have the same structure, which was not the case in Ref. [60]. Even though this was not confirmed by SPM structural measurements, this assumption is reasonable here because the DR spectra in the 3 ML regime keep the same shape than in the 1 ML regime. We therefore infer that the redshift of the 3 ML DR spectra stems from a condensed phase effect of the molecular crystal.

D. Mechanism of growth of the supramolecular assembly

We conclude on the growth mechanism of the supramolecular assembly, which is primarily driven by two types of specific interactions. On the one hand, the molecule-substrate interaction is dominated by the CN K^+ interaction. The role of this kind of interaction was evidenced in former results [38,39] and it is confirmed here by two independent observations: (i)-Curc-di(CN) molecules do not form supramolecular structures on bare Au(111), but a disordered phase and (ii) the best agreement between the experimental results and the structural model was found with the isomer whose dimensions accommodate the K^+ sites at best, which shows that isomer 2 is selected for its size. On the other hand, the molecules thus anchored to the surface keep diffusing on the ionic substrate (large domains). They are doing so in a nearly flat-lying adsorption configuration ($\simeq 30^\circ$ with respect to the surface plane) in order to favor F- π intermolecular interactions, which is the main driving process for the in-plane growth. The favorable combination between the molecule size (isomer 2), the vertical tilt angle with respect to the substrate and the distance between K^+ sites makes possible the nucleation of few molecules. This may either take place on a surface defect [2 ML KCl/Au(111)], or from the step edges (KCl bulk). Then the growth of the supramolecular assembly with a two-molecules periodic pattern forming ribbons takes place. Because the molecules have their dipole moments lying nearly in plane within the ribbons and because these grow along polar lines of the substrate, electrostatic energy may play a role in the overall adsorption configuration of the molecules ($\simeq -400$ meV). However, in this configuration, the contribution of the Coulomb interaction to the in-plane growth remains weak and is not prominent enough to promote excitonic effects in the optical absorption properties of the molecules compared to the case in solvent, as evidenced with the DR spectra. The “solvent to surface” redshift that was noticed in the DR spectra was ascribed to the fact that the absorption spectra in solvent are more representative of the optical absorption of the most stable monomer, namely, the isomer 3, whereas it is the isomer 2 which is selected by the surface to promote the supramolecular assembly.

V. CONCLUSION

We present a study dealing with the influence of the molecular design on well-adapted substrates to analyze the correlation between structural organization and optical properties of the molecules. To this end, a joint set of STM, nc-AFM, and DRS experiments on a difluoroboron complex of a curcuminoid derivative adsorbed on two different types of KCl-terminated substrates was performed. The molecules, which are polar, include CN end groups to favor their adsorption on the cationic sites of the surface. The substrates are 2 ML KCl/Au(111) and bulk KCl(001). The detailed analysis of our results proves that the molecules adsorb identically on both substrates in a supramolecular phase which is thermodynamically stable. In the monolayer regime, the molecules condense into ribbons which grow parallel to each other along the $\langle 100 \rangle_{\text{KCl}}$ or $\langle 010 \rangle_{\text{KCl}}$ polar rows of the substrate. The internal structure of the ribbons is periodic and

takes the form of an 8×2 epitaxial supercell with respect to the KCl substrate. The supercell consists of a two-molecules pattern which is stabilized by specific F- π interactions. These were identified as the main source that is steering the ordered growth of the ribbons. In this system, no intermolecular π - π interactions were identified. But it was found that, among several possible isomers, the surface selects the one whose dimensions and ability to place its CN end groups on top of K^+ species fit the best with the substrate. Intermolecular electrostatic interactions favor the adsorption of the molecules with their dipole moment aligned along $\langle 100 \rangle_{\text{KCl}}$ or $\langle 010 \rangle_{\text{KCl}}$ polar rows of the substrate. However, the in-plane electrostatic contribution is too weak to explain the ordered growth of the ribbons, which partly explains that the optical absorption of the molecules forming the ribbons are very close to those of the molecules in solvent. The DR spectra exhibit no excitonic effect due to the molecular packing, which might stem from the lack of π - π interactions in the system. Therefore,

the condensation of the molecules into a bidimensional solid phase does not modify their intrinsic optical properties. These studies were carried out in a strong methodological background where the use of (i) a potassium-based alkali halide material, (ii) a molecular dye carrying peripheral CN moieties, (iii) different types of substrates: 2 ML KCl/Au(111) and bulk KCl(001), and (iv) several joint characterization methods (STM, nc-AFM/KPFM, DRS, optical spectroscopy, and DFT), allowed us to derive the correlation between structural organization and optical properties of the molecules.

ACKNOWLEDGMENTS

The authors acknowledge the referees for their valuable insights to this work. The project leading to this publication has received funding from Excellence Initiative of Aix-Marseille University -A*MIDEX, a French “Investissements d’Avenir” programme, through the project MOLOS.

-
- [1] P. H. Lippel, R. J. Wilson, M. D. Miller, C. Wöll, and S. Chiang, *Phys. Rev. Lett.* **62**, 171 (1989).
- [2] R. J. Wilson, G. Meijer, D. S. Bethune, R. D. Johnson, D. D. Chambliss, M. S. de Vries, H. E. Hunziker, and H. R. Wendt, *Nature (London)* **348**, 621 (1990).
- [3] X. Shi, W. Brett Caldwell, Kaimin Chen, and C. A. Mirkin, *J. Am. Chem. Soc.* **116**, 11598 (1994).
- [4] J. K. Gimzewski, S. Modesti, and R. R. Schlittler, *Phys. Rev. Lett.* **72**, 1036 (1994).
- [5] T. A. Jung, R. R. Schlittler, J. K. Gimzewski, H. Tang, and C. Joachim, *Science* **271**, 181 (1996).
- [6] T. Jung, R. R. Schlittler, and J. K. Gimzewski, Conformational identification of individual adsorbed molecules with STM, *Nature (London)* **386**, 696 (1997).
- [7] V. J. Langlais, R. R. Schlittler, H. Tang, A. Gourdon, C. Joachim, and J. K. Gimzewski, *Phys. Rev. Lett.* **83**, 2809 (1999).
- [8] F. Moresco, G. Meyer, K.-H. Rieder, J. Ping, H. Tang, A. Gourdon, and C. Joachim, *Surf. Sci.* **499**, 94 (2002).
- [9] F. Rosei, M. Schunack, P. Jiang, A. Gourdon, E. Laegsgard, I. Stensgaard, C. Joachim, and F. Besenbacher, *Science* **296**, 328 (2002).
- [10] M. Stöhr, M. Gabriel, and R. Möller, *Europhys. Lett.* **59**, 423 (2002).
- [11] S. Berner, M. de Wild, L. Ramoïno, S. Ivan, A. Baratoff, H.-J. Gütherodt, H. Suzuki, D. Schlettwein, and T. A. Jung, *Phys. Rev. B* **68**, 115410 (2003).
- [12] J. V. Barth, *Annu. Rev. Phys. Chem.* **58**, 375 (2007).
- [13] A. Kühnle, *Curr. Opin. Colloid Interface Sci.* **14**, 157 (2009).
- [14] L. Gross, F. Mohn, N. Moll, and G. Meyer, *Science* **325**, 1110 (2009).
- [15] J. Repp, G. Meyer, S. M. Stojković, A. Gourdon, and C. Joachim, *Phys. Rev. Lett.* **94**, 026803 (2005).
- [16] L. Nony, R. Bennewitz, O. Pfeiffer, E. Gnecco, A. Baratoff, E. Meyer, T. Eguchi, A. Gourdon, and C. Joachim, *Nanotechnology* **15**, S91 (2004).
- [17] L. Nony, E. Gnecco, A. Baratoff, A. Alkauskas, R. Bennewitz, O. Pfeiffer, S. Maier, A. Wetzel, E. Meyer, and C. Gerber, *Nano Lett.* **4**, 2185 (2004).
- [18] S. A. Burke, J. M. Mativetsky, R. Hoffmann, and P. Grütter, *Phys. Rev. Lett.* **94**, 096102 (2005).
- [19] S. A. Burke, J. M. Mativetsky, S. Fostner, and P. Grütter, *Phys. Rev. B* **76**, 035419 (2007).
- [20] J. M. Mativetsky, S. A. Burke, S. Fostner, and P. Grütter, *Small* **3**, 818 (2007).
- [21] S. A. Burke, W. Ji, J. M. Mativetsky, J. M. Topple, S. Fostner, H.-J. Gao, H. Guo, and P. Grütter, *Phys. Rev. Lett.* **100**, 186104 (2008).
- [22] S. Maier, L.-A. Fendt, L. Zimmerli, T. Glatzel, O. Pfeiffer, F. Diederich, and E. Meyer, *Small* **4**, 1115 (2008).
- [23] S. A. Burke, J. M. LeDue, Y. Miyahara, J. M. Topple, S. Fostner, and P. Grütter, *Nanotechnology* **20**, 264012 (2009).
- [24] S. A. Burke, J. M. Topple, and P. Grütter, *J. Phys.: Condens. Matter* **21**, 423101 (2009).
- [25] S. A. Burke, J. M. LeDue, J. M. Topple, S. Fostner, and P. Grütter, *Adv. Mater.* **21**, 2029 (2009).
- [26] J. Schütte, R. Bechstein, M. Rohlfling, M. Reichling, and A. Kühnle, *Phys. Rev. B* **80**, 205421 (2009).
- [27] J. M. Topple, S. A. Burke, W. Ji, S. Fostner, A. Tekiel, and P. Grütter, *J. Phys. Chem. C* **115**, 217 (2011).
- [28] J. Repp, S. Fölsch, G. Meyer, and K.-H. Rieder, *Phys. Rev. Lett.* **86**, 252 (2001).
- [29] J. Repp, G. Meyer, F. E. Olsson, and M. Persson, *Science* **305**, 493 (2004).
- [30] L. Gross, F. Mohn, P. Liljeroth, J. Repp, F. J. Giessibl, and G. Meyer, *Science* **324**, 1428 (2009).
- [31] H. Walch, T. Leoni, O. Guillermet, V. Langlais, A. Scheuermann, J. Bonvoisin, and S. Gauthier, *Phys. Rev. B* **86**, 075423 (2012).
- [32] J. Chen, J. Guo, X. Meng, J. Peng, J. Sheng, L. Xu, Y. Jiang, X.-Z. Li, and E.-G. Wang, *Nat. Commun.* **5**, 4056 (2014).

- [33] S. Schintke, S. Messerli, M. Pivetta, F. Patthey, L. Libioulle, M. Stengel, A. De Vita, and W.-D. Schneider, *Phys. Rev. Lett.* **87**, 276801 (2001).
- [34] X. H. Qiu, G. V. Nazin, and W. Ho, *Science* **299**, 542 (2003).
- [35] G. Kresse, M. Schmid, E. Napetschnig, M. Shishkin, L. Köhler, and P. Varga, *Science* **308**, 1440 (2005).
- [36] R. Pawlak, L. Nony, F. Bocquet, V. Oison, M. Sassi, J.-M. Debierre, C. Loppacher, and L. Porte, *J. Phys. Chem. C* **114**, 9290 (2010).
- [37] F. Bocquet, L. Nony, S. C. B. Mannsfeld, V. Oison, R. Pawlak, L. Porte, and C. Loppacher, *Phys. Rev. Lett.* **108**, 206103 (2012).
- [38] A. Amrous, F. Bocquet, L. Nony, F. Para, Ch. Loppacher, S. Lamare, F. Palmino, F. Cherioux, D. Z. Gao, F. F. Canova, M. B. Watkins, and A. L. Shluger, *Adv. Mater. Interfaces* **1**, 1400414 (2014).
- [39] J. Gaberle, D. Z. Gao, A. L. Shluger, A. Amrous, F. Bocquet, L. Nony, F. Para, Ch. Loppacher, S. Lamare, and F. Cherioux, *J. Phys. Chem. C* **121**, 4393 (2017).
- [40] K^+ and Cl^- ionic radii are 152 and 167 pm, respectively.
- [41] M. Müller, J. Ikonov, and M. Sokolowski, *Surf. Sci.* **605**, 1090 (2011).
- [42] C. Marquardt, A. Paulheim, and M. Sokolowski, *Surf. Sci.* **641**, 128 (2015).
- [43] C. Loppacher, U. Zerweck, and L. M. Eng, *Nanotechnology* **15**, S9 (2004).
- [44] S. Koslowski, D. Rosenblatt, A. Kabakchiev, K. Kuhnke, K. Kern, and U. Schlickum, *Beilstein J. Nanotechnol.* **8**, 1388 (2017).
- [45] V. Kisand, A. Kikas, E. Kukk, E. Nommiste, K. Kooser, T. Kaeaembre, R. Ruus, M. Valden, M. Hirsimaki, and P. Jussila, *J. Phys.: Condens. Matter* **20**, 145206 (2008).
- [46] U. Barjenbruch and M. Henzler, *Surf. Sci.* **211**, 749 (1989).
- [47] S. F. Tsay, J. Y. Chung, M.-F. Hsieh, S. S. Ferng, C.-T. Lou, and D. S. Lin, *Surf. Sci.* **603**, 419 (2009).
- [48] I. Beinik, C. Barth, M. Hanbücken, and L. Masson, *Sci. Rep.* **5**, 8223 (2015).
- [49] M. Henzler, C. Homann, U. Malaske, and J. Wollschläger, *Phys. Rev. B* **52**, R17060(R) (1995).
- [50] J. Baker and P. A. Lindgard, *Phys. Rev. B* **60**, 16941 (1999).
- [51] J. D. E. McIntyre and D. E. Aspnes, *Surf. Sci.* **24**, 417 (1971).
- [52] H. Proehl, R. Nitsche, Th. Dienel, K. Leo, and T. Fritz, *Phys. Rev. B* **71**, 165207 (2005).
- [53] T. Dienel, C. Loppacher, S. C. B. Mannsfeld, R. Forker, and T. Fritz, *Adv. Mater.* **20**, 959 (2008).
- [54] R. Forker, M. Gruenewald, and T. Fritz, *Annu. Rep. Prog. Chem., Sect. C: Phys. Chem.* **108**, 34 (2012).
- [55] M. Müller, A. Langner, O. Krylova, E. Le Moal, and M. Sokolowski, *Appl. Phys. B* **105**, 67 (2011).
- [56] B. Doppagne, M. C. Chong, H. Bulou, A. Boeglin, F. Scheurer, and G. Schull, *Science* **361**, 251 (2018).
- [57] B. Doppagne, T. Neuman, R. Soria-Martinez, L. E. Parra López, H. Bulou, M. Romeo, S. Berciaud, F. Scheurer, J. Aizpurua, and G. Schull, *Nat. Nanotechnol.* **15**, 207 (2020).
- [58] M. Müller, A. Paulheim, C. Marquardt, and M. Sokolowski, *J. Chem. Phys.* **138**, 064703 (2013).
- [59] M. Müller, A. Paulheim, A. Eisfeld, and M. Sokolowski, *J. Chem. Phys.* **139**, 044302 (2013).
- [60] F. Bocquet, L. Nony, F. Para, P. Luangprasert, J.-V. Naubron, Ch. Loppacher, T. Leoni, A. Thomas, A. Ranguis, A. d'Aléo, F. Fages, and C. Becker, *Phys. Rev. B* **97**, 235434 (2018).
- [61] K. Stahrenberg, Th. Herrmann, K. Wilmers, N. Esser, W. Richter, and M. J. G. Lee, *Phys. Rev. B* **64**, 115111 (2001).
- [62] S. Babar and J. H. Weaver, *Appl. Opt.* **54**, 477 (2015).
- [63] M. Pröhl, U. S. Schubert, W. Weigand, and M. Gottschaldt, *Coord. Chem. Rev.* **307**, 32 (2016).
- [64] M. Halik, W. Wenseleers, C. Grasso, F. Stellacci, E. Zojer, S. Barlow, J.-L. Brédas, J. W. Perry, and S. R. Marder, *Chem. Commun.* **13**, 1490 (2003).
- [65] E. Cogy-Laage, J.-F. Allemand, O. Ruel, J.-B. Baudin, V. Croquette, M. Blanchard-Desce, and L. Jullien, *Chem.-Eur. J.* **10**, 1445 (2004).
- [66] K. Ono, K. Yoshikawa, Y. Tsuji, H. Yamaguchi, R. Uozumi, M. Tomura, K. Tagaa, and K. Saito, *Tetrahedron* **63**, 9354 (2007).
- [67] S. Xu, R. E. Evans, T. Liu, G. Zhang, J. N. Demas, C. O. Trindleand, and C. L. Fraser, *Inorg. Chem.* **52**, 3597 (2013).
- [68] T. Butler, W. A. Morris, J. Samonina-Kosicka, and C. L. Fraser, *ACS Appl. Mater. Interface* **8**, 1242 (2016).
- [69] F. P. Macedo, C. Gwengo, S. V. Lindeman, M. D. Smith, and J. R. Gardinier, *Eur. J. Inorg. Chem.* **2008**, 3200 (2008).
- [70] C. Qian, G. Hong, M. Liu, P. Xue, and R. Lu, *Tetrahedron* **70**, 3935 (2014).
- [71] A. Felouat, A. d'Aléo, and F. Fages, *J. Org. Chem.* **78**, 4446 (2013).
- [72] G. Bai, C. Yu, C. Cheng, E. Hao, Y. Wei, X. Mu, and L. Jiao, *Org. Biomol. Chem.* **12**, 1618 (2014).
- [73] M. Rivoal, E. Zaborova, G. Canard, A. d'Aléo, and F. Fages, *New J. Chem.* **40**, 1297 (2016).
- [74] A. d'Aléo, A. Felouat, V. Heresanu, A. Ranguis, D. Chaudanson, A. Karapetyan, M. Giorgi, and F. Fages, *J. Mater. Chem. C* **2**, 5208 (2014).
- [75] K. Kamada, T. Namikawa, S. Senatore, C. Matthews, P.-F. Lenne, O. Maury, C. Andraud, M. Ponce-Vargas, B. LeGuennic, D. Jacquemin, P. Agbo, D. D. An, S. S. Gauny, X. Liu, R. J. Abergel, F. Fages, and A. D'Aléo, *Chem. Eur. J.* **22**, 5219 (2016).
- [76] J. Fabian and H. Hartmann, *J. Phys. Org. Chem.* **17**, 359 (2004).
- [77] C. Risko, E. Zojer, P. Brocorens, S. R. Marder, and J.-L. Brédas, *Chem. Phys.* **313**, 151 (2005).
- [78] B. Domercq, C. Grasso, J.-L. Maldonado, M. Halik, S. Barlow, S. R. Marder, and B. Kippelen, *J. Phys. Chem. B* **108**, 8647 (2004).
- [79] K. Ono, J. Hashizume, H. Yamaguchi, M. Tomura, J. i. Nishida, and Y. Yamashita, *Org. Lett.* **11**, 4326 (2009).
- [80] M. S. Wrackmeyer, M. Hummert, H. Hartmann, M. K. Riedeand, and K. Leo, *Tetrahedron* **66**, 8729 (2010).
- [81] E. Kim, A. Felouat, E. Zaborova, J.-C. Ribierre, J. Weon Wu, S. Senatore, C. Matthews, P.-F. Lenne, C. Baffert, A. Karapetyan, M. Giorgi, D. Jacquemin, M. Ponce-Vargas, B. Le Guennic, F. Fages, and A. d'Aléo, *Org. Biomol. Chem.* **14**, 1311 (2016).
- [82] G. Canard, M. Ponce-Vargas, D. Jacquemin, B. Le Guennic, A. Felouat, M. Rivoal, E. Zaborova, A. d'Aléo, and F. Fages, *RSC Adv.* **7**, 10132 (2017).
- [83] A. D. Becke, *J. Chem. Phys.* **98**, 5648 (1993).

- [84] Gaussian 16, Revision C.01, M. J. Frisch, G. W. Trucks, H. B. Schlegel, G. E. Scuseria, M. A. Robb, J. R. Cheeseman, G. Scalmani, V. Barone, G. A. Petersson, H. Nakatsuji, X. Li, M. Caricato, A. V. Marenich, J. Bloino, B. G. Janesko, R. Gomperts, B. Mennucci, H. P. Hratchian, J. V. Ortiz, A. F. Izmaylov *et al.*, Gaussian, Inc., Wallingford, CT, 2016.
- [85] F. Neese, *Wiley Interdiscip. Rev.: Comput. Mol. Sci.* **2**, 73 (2012).
- [86] D. Necas and P. Klapetek, *Cent. Eur. J. Phys.* **10**, 181 (2012).
- [87] F. J. Giessibl and H. Bielefeldt, *Phys. Rev. B* **61**, 9968 (2000).
- [88] I. Horcas, R. Fernández, J. M. Gómez-Rodríguez, J. Colchero, J. Gómez-Herrero, and A. M. Baro, *Rev. Sci. Instrum.* **78**, 013705 (2007).
- [89] H. Zaglmayr, C. G. Hu, L. D. Sun, and P. Zeppenfeld, *Meas. Sci. Technol.* **25**, 115603 (2014).
- [90] See, <https://amubox.univ-amu.fr/s/4YRR2StjtGoaPGm>.
- [91] F. E. Olsson, M. Persson, J. Repp, and G. Meyer, *Phys. Rev. B* **71**, 075419 (2005).
- [92] X. Sun, M. P. Felicissimo, P. Rudolf, and F. Silly, *Nanotechnology* **19**, 495307 (2008).
- [93] Q. Guo, Z. Qin, C. Liu, K. Zang, Y. Yu, and G. Cao, *Surf. Sci.* **604**, 1820 (2010).
- [94] H.-C. Ploigt, C. Brun, M. Pivetta, F. Patthey, and W.-D. Schneider, *Phys. Rev. B* **76**, 195404 (2007).
- [95] 3 Å within 12 h at 4.8 K.
- [96] P. Li, J. M. Maier, E. C. Vik, C. J. Yehl, B. E. Dial, A. E. Rickher, M. D. Smith, P. J. Pellechia, and K. D. Shimizu, *Angew. Chem. Int. Ed.* **56**, 7209 (2017).
- [97] S. Kawahara, S. Tsuzuki, and T. Uchimaru, *J. Phys. Chem. A* **108**, 6744 (2004).
- [98] A. Felouat, A. d'Aléo, A. Charaf-Eddin, D. Jacquemin, B. Le Guennic, E. Kim, K. J. Lee, J. H. Woo, J.-C. Ribierre, J. W. Wu, and F. Fages, *J. Phys. Chem. A* **119**, 6283 (2015).
- [99] M. Kasha, *Radiat. Res.* **20**, 55 (1963).
- [100] M. Kasha, H. R. Rawls, and M. Ashraf El-Bayoumi, *Pure Appl. Chem.* **11**, 371 (1965).
- [101] A. Davydov, *The Theory of Molecular Excitons* (Springer, New York, 1971).
- [102] J. S. Briggs and A. Herzenberg, *Mol. Phys.* **21**, 865 (1971).
- [103] A. Eisfeld and J. S. Briggs, *Chem. Phys.* **281**, 61 (2002).
- [104] A. Eisfeld and J. S. Briggs, *Chem. Phys.* **324**, 376 (2006).
- [105] F. C. Spano, *Chem. Phys.* **325**, 22 (2006).
- [106] A. S. Davydov, *Zh. Eksp. Teor. Fiz.* **18**, 210 (1948) [*Ukr. J. Phys.* **53**, 65 (2008)].
- [107] F. C. Spano, *Acc. Chem. Res.* **43**, 429 (2010).
- [108] F. C. Spano and C. Silva, *Annu. Rev. Phys. Chem.* **65**, 477 (2014).
- [109] N. J. Hestand and F. C. Spano, *Chem. Rev.* **118**, 7069 (2018).
- [110] M. Hochheim and T. Bredow, *J. Comput. Chem.* **36**, 1805 (2015).
- [111] V. M. Agranovich and G. F. Bassani, *Thin Films and Nanostructures: Electronic Excitations in Organic Based Nanostructures*, Vol. 31 (Elsevier, Amsterdam, 2003).